PAPER

Check for updates

Structured aqueous processed lignin-based NMC cathodes for energy-dense LIBs with improved rate capability†

Silje Nornes Bryntesen, [iD] [a] Per Håkon Finne,[b] Ann Mari Svensson, [iD] [b] Paul R. Shearing, [iD] [ac] Nikolai Tolstik,[ef] Irina T. Sorokina,[ef] Jakob Vinje,[d] Jacob Joseph Lamb [iD] [a] and Odne Stokke Burheim*[a]

The cost and environmental impact of lithium-ion batteries (LIBs) can be reduced substantially by enabling the aqueous processing of cathode materials. For the first time, we fabricate high-density, thick NMC111 cathode coatings using water as a solvent, and bio-derived kraft lignin as a binder material. The performance deterioration at high discharge currents is amplified by high mass loading and low bulk porosity. At porosities higher than 60%, the electronic conductivity limits the rate capability of the cathode, while for porosities lower than 30%, ionic conduction causes significant ionic polarization and consequently diminishes rate performance. The underlying lithium-ion diffusion limitation at current densities higher than 0.2 C is mitigated by creating line structures on the surface of the cathode. Structuring the half-dried cathode surface with ceramic blades is preferred over a stamp-like silicon wafer, and the line structures are easier to produce with high mechanical stability in comparison to pit structures. The lignin/water cells investigated herein restore after undergoing rate capability tests (5C), except those with pit structures or ultra-high thickness (>200 μm), due to the extensive crack formation during water evaporation which causes poor mechanical stability. Mechanical and laser structuring methods are compared on the surface of a PVDF/NMP-based cathode. Concerning the implementation in a large-scale battery factory, mechanical structuring is currently considered a processing of choice as it has no surface residuals or waste material. However, laser structuring with ultra-short pulses technique has the potential of outperforming mechanical structuring if the process is optimized to high precision to reduce residual and waste material, due to reproducibility and lower operational costs.

[a]*Department of Energy and Process Engineering, Norwegian University of Science and Technology, Kolbjørn Hejes Vei 1B, No-7034 Trondheim, Norway. E-mail: odne.s. burheim@ntnu.no; silje.n.bryntesen@ntnu.no*

[b]*Department of Materials Science and Engineering, Norwegian University of Science and Technology, Sem Sælands Vei 12, 7491 Trondheim, Norway*

[c]*University College London, Gower St., London, England*

[d]*NTNU Nanolab, Sem Sælands Vei 14, 7491 Trondheim, Norway*

[e]*Department of Physics, Norwegian University of Science and Technology, Høgskoleringen 5, 7491 Trondheim, Norway*

[f]*ATLA Lasers AS, Richard Birkelands Vei 2B, 7491 Trondheim, Norway*

† Electronic supplementary information (ESI) available. See DOI: https://doi.org/10.1039/d2ta08606a

1 Introduction and outline

Currently, wet-slurry electrode production is an energy-intensive step in the fabrication of lithium-ion batteries (LIB).[1] The anode is produced using a sustainable cellulose-based CMC binder and water as a solvent, while the NMC cathode still uses a polyvinylidene fluoride (PVDF) binder in tandem with the highly flammable and toxic *N*-methyl-2-pyrrolidone (NMP) solvent. Additional ventilation and solvent recovery are therefore required for the cathode fabrication process. Replacing the costly PVDF cathode binder with water-soluble binders will simplify the recycling process for end-of-life LIBs, by mitigating the conversion from solid-coated cathodes to aqueous black mass.[2] Facilitating the aqueous processing of NMC cathodes would reduce production costs and energy consumption while improving sustainability. This has motivated many recent studies to develop suitable water-compatible binder materials for cathodes.[3–8]

Ponnuchamy *et al.*[9] recently compared the binding ability of sustainable cellulose-based and unsustainable binders to graphene sheets, demonstrating that lignin offers the highest binding strength. However, little research has examined lignin's capacity to bind with active cathode materials and aluminum (Al) current collectors. It is expected that lignin can provide strong cohesion and adhesion forces to electrode components since there are 2–5% carbon black in conventional cathodes, which can be fabricated with a carbon-coated aluminum foil (C–Al).[10,11] These attributes ultimately demonstrate that lignin can play a key role in enabling a transition toward the aqueous fabrication of LIB cathodes.

This journal is © The Royal Society of Chemistry 2023

J. Mater. Chem. A, 2023, **11**, 6483–6502 | 6483

Lignin is a waste material from the pulp industry, therefore it is inexpensive and abundant,[12,13] and can serve as a promising bio-derived water-soluble binder material. It also possesses a higher electrical conductivity compared to its commercial PVDF counterpart.[14] The molecular structure of lignin is complex, and its characteristics depend on how it is pre-treated (kraft, soda, or steam exploded) and whether it is derived from softwood (poplar) or hardwood (pine).[13,15,16] It has been researched as a precursor for the production of various battery components,[7] including separators, conductive additives, activated carbon for capacitors,[17] electrolytes,[18] and binder materials.[1,9,19,20] Lignin has also been implemented as a precursor for hard carbon in LIB anodes, but is seldom reported as a functional binder material in LIB electrodes, especially for cathodes.[6] Lu et al.[19] conducted one of the few studies to report the electrochemical cycling performance of lignin as a binder material in LIB cathodes, and obtained promising discharge capacities of 148 mA h g^{-1} and 300 mA h g^{-1} for the LiFePO$_4$ (LFP) cathode and graphite anode, respectively. The LFP cathodes are compatible with water; however, problems arise when using Ni-containing NMC cathodes.[21]

When NMC is exposed to humid air or water, H$_2$O and CO$_2$ can be adsorbed onto the NMC surface, interact with Ni and Li, and eventually form lithium carbonates (Li$_2$CO$_3$ or LiHCO$_3$) and lithium hydroxide (LiOH) surface layers.[22–24] During the aqueous production step, Li$^+$ leach out from the particle surface and exchange with H$^+$, which alkalizes the water and increases the pH.[24–26] When water evaporates, LiOH, LiHCO$_3$, and Li$_2$CO$_3$ are left on the surface of the NMC.[21] Although there is some disagreement in the literature regarding the extent to which this phenomenon affects cycling performance,[24] researchers generally agree that the severity of surface layer formation and Li$^+$-leaching increases with Ni content when going from NMC111 to NMC811, while the bulk remains unchanged.[21,24]

For the Ni-rich NMC811, H$^+$/Li$^+$-exchange occurs, and a 10 nm surface layer is consequently formed.[27] The formation of surface layers has a negative impact on the electrode's initial discharge capacity and coulombic efficiency and can cause capacity degradation over long-term cycling. However, researchers have proposed that the H$^+$/Li$^+$-exchange is partially reversible due to re-lithiation upon subsequent cycles.[27,28] Shkrob et al.[29] proposed that cation exchange occurs on the edges of the active powder and intercalant H$^+$ can be swapped back with Li$^+$ during cycling. This is believed to be detrimental over long-term cycling because the presence of H$^+$ can react with fluorine in the electrolyte and form hydrofluoric acid (HF).

Recent reports suggest that NMC111 experiences Li$^+$-leaching and Li$^+$/H$^+$-exchange, but forms minor surface residuals. For example, Jung et al.[27] compared the storage capacity of NMC111 and NMC811, and showed that the surface of the former remained unchanged under ambient conditions over the duration of one year. This result agrees with a recent study on the aqueous production of NMC111 using lignin as a binder, where X-ray Photoelectron Spectroscopy (XPS) revealed no significant formation of surface residuals.[30] However, pH measurements determined that Li$^+$-leaching and Li$^+$/H$^+$ exchange occurs,[21,30] and the presence of H$^+$ in the electrolyte is considered to be one of the main issues after exposing NMC111 particles to water. However, the different binder materials and mixing procedures often make it challenging to distinguish whether the decreasing capacity is a result of the water exposure or the binder itself.[21]

If kraft lignin with alkali residuals (sodium hydroxide (NaOH) and sodium sulfate (Na$_2$S)) are mixed with water, these residuals dissolve, which increases the pH to between 9–11. At this pH, the phenolic hydroxyl groups on lignin are activated, making lignin soluble in water.[30,31] These species are present in small amounts, and Na is often used as an additive in CMC binders (Na-CMC) for cathodes and anodes,[22,32] and its presence is not considered to be detrimental to the battery.[1] Conversely, a high pH may cause corrosion of the aluminum current collector,[25] but such an outcome can be avoided by using a carbon-coated aluminum (C–Al) current collector.[11] An extensive explanation of this matter is found in our recent work based on,[30] which is about to be published.

The battery industry aims for higher energy densities and lower manufacturing costs by increasing electrode mass loading.[33] Finding a binder that provides high mechanical stability is becoming increasingly important. Compact and mechanically stable electrode coatings possessing high thicknesses can be realized with the proper binder and fabrication procedure. The aqueous processing of cathode coatings with high mass loading is particularly problematic due to extensive cracking associated with high capillary pressure during water evaporation.[34,35]

Thick electrode coatings induce transport limitations within the electrode since Li$^+$ cannot penetrate the deeper layers of the electrode coating.[36] The elongation of the Li$^+$ diffusion path leads to a drop in performance during fast charging and discharging, and ultimately restricts rate capability.[37] Hu et al.[38] studied the rate-limiting steps of high-density (22 mg cm^{-2}) Ni-rich PVDF/NMP-based cathodes and reported several mechanisms responsible for poor rate capability. Firstly, at the lattice level, the phase conversion between H1 and M phases was kinetically slower than other phase transitions and thus became the rate-limiting step from low to moderate current densities. When increasing the C-rate, all phase conversions in the dQ/dV plot became sluggish, and the kinetics of the electrochemical reaction was controlled by both transport and kinetics. Secondly, they reported the rate capability of thick electrodes is governed by the porosity, as the porosity affects both electronic and ionic conductivity, in an adverse manner.

The porosity of electrodes can be controlled by calendering, and the preferred value for PVDF-based cathodes is generally between 30–40%.[39,40] At a porosity higher than 40%, the electronic conductivity determines the rate performance, because disconnected ion flow channels (pores) in the cathode coating introduce polarization.[38] When reducing the porosity to less than 30%, ionic conduction within thick and dense cathodes (22 mg cm^{-2}) was shown to become rate-limiting, resulting in significant transport polarization and poor rate performance.

Various approaches have been utilized to engineer electrode architectures to increase the battery's rate capability. This includes introducing voids or macro-pores to the electrode

6484 | J. Mater. Chem. A, 2023, 11, 6483–6502

This journal is © The Royal Society of Chemistry 2023

coating, magnetic alignment of particles,[41–43] controlled mud-cracking,[44] freeze casting,[45–48] pore former inclusion,[49] surface doping,[50] and co-extrusion methods.[51] An extensive review of these processes is available in the study undertaken by Usseglio-Viretta et al.[52]

Multiple researchers are developing techniques to reduce the solid diffusion path in anodes and cathodes by increasing the active particle surface area with smaller particles,[53–55] or by structuring the electrode surface area with micro-channels.[36,55–58] The surface-induced structures will lower the tortuosity pathways for facile Li⁺-transport deep into the electrode, limit electrolyte concentration gradients, and reduce the electrochemical overpotential that leads to Li-plating. These features will eventuate higher rate capabilities.[57] Fig. 1 illustrate how the Li⁺-diffusion pathway for an unstructured cathode (red) are shortened after surface structuring (yellow).

Much research has focused on structuring the graphite-based anodes which consists of graphite flakes creating a higher anisotropy (i.e. tortuosity), and therefore a low Li⁺-conductivity, compared to the cathode with mainly spherical transition metal oxide particles.[55,56] However, structuring is compatible with most known cathode chemistries, such as $LiFePO_2$ (LFP),[59–61] $LiMnO_2$ (LMO),[62] and $LiNiMnCoO_2$ (NMC).[26,53,57,58,63]

When comparing different variations of unstructured and structured electrodes in full cells, it is found that structuring both electrode coatings[58] or only the cathode[57] is preferred for optimal cycling performance at high C-rates. Recently, Park et al.[64] fabricated $LiCoO_2$ (LCO) cathode and graphite anodes with ultra-high thicknesses of 700 μm and 650 μm, respectively, and showed that structuring improved the rate capability at high current densities. In addition to increasing the rate capability, surface structuring has proven to shorten the electrolyte wetting time.[37,40] Plateau et al. experimented with microcast-structuring on ultrathick (37 mg cm⁻²) graphite anodes and NMC811 cathodes. Structuring increased the specific capacity (40%) and areal capacity (30%) over 200 cycles as the structures facilitated a short Li⁺-diffusion path; this greatly reduced concentration differences and stress accumulation within thick

coatings and ultimately improved the coating's mechanical strength.[36]

Amongst the most common structuring techniques are additive/subtractive manufacturing and ex situ/in situ templating methods.[33] Laser structuring/patterning is a fast method with high precision; however, laser ablation with nanosecond long pulses may form residuals and generate extensive waste material as a result of it being a subtractive method. This consequently increases yield and cost and presents additional challenges for large-scale production.[65]

Nanosecond pulsed lasers have been utilized earlier to pattern electrodes due to an extremely short duration of their pulses produces ablation with minimal heat input to the surrounding material. Using ultra-short pulse lasers (pico-second or femtosecond) in the mid-IR eliminates the scalability issues as these lasers allow for further optimization of heat input, waste material, and efficiency.[57] Alternatively, mechanical structuring method completely eliminates waste materials, and can be implemented in tandem with calendering without disrupting the casting process. No chemical changes are introduced to the system because mechanical forces acting perpendicular to the electrode coating compresses the surface into a predefined topographical pattern. This creates local discrepancies in the pore distribution of the electrode coating, as illustrated in Fig. 2. For simplicity, the literature typically reports the average porosity of the total electrode coating without accounting for variations in these compressed areas. Therefore, the average porosity is evaluated as the mean between the bulk and compacted electrode areas.

Although the compressed electrode reduces the diffusion path length for Li⁺, it may limit the infiltration of electrolyte into the pores and thus increase the tortuosity in the compressed area.[37] Such increases in local tortuosity impair ionic transport and may cause lower rate capabilities. The geometry of the structures, such as spacing, width, and depth, needs to be optimized to avoid unnecessary removal of electrode material, although large spacing and limited indentation depth have also
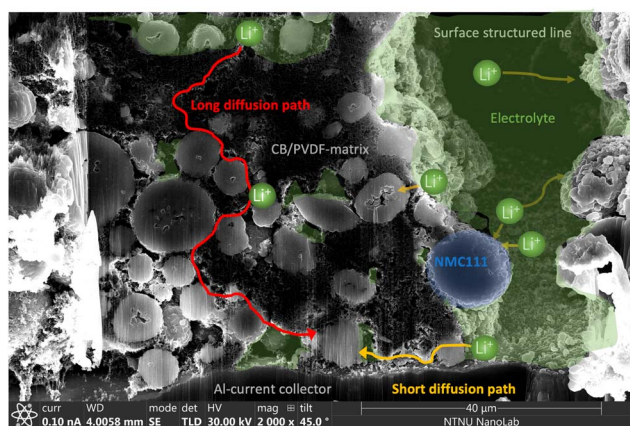

Fig. 1 The cross-section of an NMC cathode induced with a structured line. The Li⁺-diffusion pathway for an unstructured cathode (red) are shortened after surface structuring (yellow).
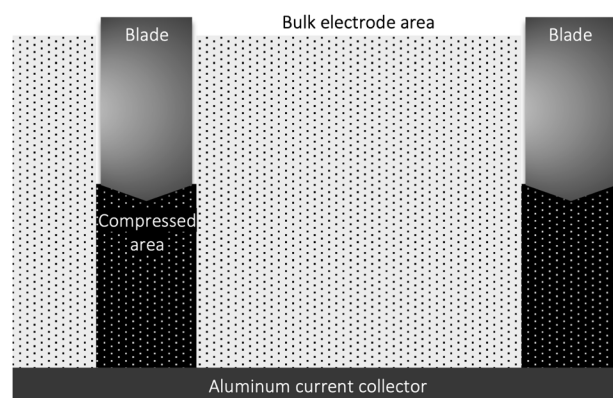

Fig. 2 Illustration of the cross-section of an electrode after electrode material is compressed by mechanical structuring. The porosity in the electrode bulk area is termed the bulk porosity, whereas the porosity for the whole electrode (including the compressed area and the bulk area) is defined as the average porosity.

increased Li$^+$-transport.[40,66] Nonetheless, electrodes with local porosity differences have demonstrated enhanced rate capabilities at high current densities, because Li$^+$ have increased accessibility in areas around the indentations.[66] Literature reviews have been conducted to illuminate opportunities and challenges for different structures,[33,67] but few have compared several structuring methods and patterns experimentally.

Furthermore, little research has been performed on the structuring of thick aqueous processed NMC cathodes to attain high energy, and power densities.[26] Numerical models and experimental techniques were recently combined to characterize laser-patterned graphite anodes and NMC622 cathodes with commercially relevant thicknesses (110 μm).[57] However, structuring cathodes with thickness >110 μm and mass loading >12 mg cm^{-2}, combined with aqueous binders beyond the commercial CMC and acrylic-based, is yet to be tested.[57]

In the current study, we investigate the electrochemical rate performance of unstructured and laser-structured NMC111 cathode coatings fabricated using PVDF/NMP or lignin/water as a binder/solvent. Firstly, PVDF/NMP cathodes with low (L), medium (M), and high (H) mass loading (ML) are calendered to different porosities and thicknesses, and structured mechanically, to reveal the optimal conditions to achieve a high rate capability. The PVDF/NMP cathodes with medium mass loading (M-ML) are laser structured (laser-LL) and compared to those structured mechanically using steel blades (BladePerf-VLL). The most robust structuring method is used for structuring lignin/water cathodes. The lignin/water-based cathodes with medium mass loading (M-ML) are first calendered to different porosities to reveal the optimal rate capability. Lignin/water-based cathodes with constant porosity (40–45%) and low (LT), medium (MT), high (HT), and ultra-thick (UT) cathode coatings are fabricated and structured mechanically using blades (BladePerf-LL) and a silicon wafer stamp. For the silicon wafer stamp, two types of structured patterns were tested electrochemically: lines (L) or pits (P) with large (L) or small (S) distances between the structures. All cathodes are tested electrochemically under high current densities, and the structures are analyzed using Scanning Electron Microscopy with Energy Dispersive Spectroscopy (SEM/EDS) after structuring, cell assembly, and cycling (post-mortem).

2 Experimental

2.1 Cathode slurry mixing and coating

Two types of NMC111 cathodes were tested: one slurry was fabricated using a pre-mixed binder/solvent dispersion with PVDF/NMP (1 : 20 PVDF : NMP wt%), and the other was produced using a pre-mixed lignin/water dispersion (1 : 10 wt% lignin : water). The ratio between NMC111 : Carbon black : binder was 90 : 5 : 5 wt%. Information on the chemicals used is found in ESI Table S6.† The PVDF/NMP-based cathode slurries were mixed with a planetary centrifugal mixer (THINKY Corp., ARE-250) for 25 min at 1500 rpm, followed by 5 min at 2000 rpm at room temperature (RT). The lignin/water-based slurries were mixed at 1000 rpm (10 min) and 2000 rpm (10 min) and repeated three times, resulting in a total mixing time of 60

minutes to avoid carbon agglomeration. The slurries were tape-casted (MTI Corp., MSK-AFA-HC100) onto an aluminum (Al)-foil (15 μm) (the PVDF/NMP slurries), or carbon-coated Al (C–Al) foil (the lignin/water slurries) using a doctor blade at a 20 s^{-1} coating speed and a gap size varying between 200-600 μm to create cathodes with different mass loading. All electrode sheets were dried in a vacuum overnight at 50 °C (for lignin/water slurries) or 90 °C (for PVDF/NMP slurries) to ensure proper solvent evaporation, as explained in our previous paper.[30] Furthermore, the mechanically perforated cathodes (BladePerf-VLL) were coated onto a pre-cut Ti-foil (134 μm thick) instead of an Al-foil or C–Al foil.

2.2 Electrode porosity

The porosity is defined as the ratio between the volume of the pores in the electrode and the total volume of the electrode itself, and is calculated using:

$$\text{Porosity}[\%] = \frac{V - W\left[\frac{C_{\text{NMC}}}{\rho_{\text{NMC}}} + \frac{C_{\text{Binder}}}{\rho_{\text{Binder}}} + \frac{C_{\text{Carbon\ black}}}{\rho_{\text{Carbon\ black}}}\right]}{V} \times 100 \tag{1}$$

where V is the total volume of the electrode, C is the ratio of each material in the electrode, W is the weight per unit area (loading), and ρ is the density of each material.[66] The porosity was controlled by calendering.

The porosity varied for the different structuring methods, and it is necessary to define the terms average porosity and bulk porosity. The average porosity is defined as the overall porosity across the total electrode volume, including the empty volume arising from the structures, and is calculated using eqn (1). The term bulk porosity is used to describe the porosity of the areas between the structures and does not include the empty volume resembling the structures.

The bulk porosity between the structures should remain unchanged after laser and mechanical structuring. For a laser-structured electrode, the average porosity calculated from eqn (1) is increased while the weight is reduced, since it is a subtractive method, and the volume used in the porosity calculation remains constant. However, for the mechanically structured cathodes with no material removal, the cathode's average porosity remains unchanged. The local porosity variations are altered, and the porosity under the embossed structures is reduced by compressive forces, as illustrated in Fig. 2.

2.3 Cathode surface structuring

The cathode surfaces were structured with: (1) laser (PVDF/NMP-cathodes) or (2) compressive force using steel blades (PVDF/NMP-cathodes), ceramic blades (lignin/water-cathodes), or a structured silicon wafer (lignin/water-cathodes). Each method created different structure patterns (lines (L) or pits (P)) and structure dimensions. The dimensions were defined by either the indentation width (lines) or diameter (pits), the spacing between the indentations, and the indentation depth relative to the total coating thickness (%) (Table 1).

6486 | *J. Mater. Chem. A*, 2023, **11**, 6483–6502

This journal is © The Royal Society of Chemistry 2023

Table 1 Overview of the binder/solvents, structuring tools, and the structured patterns tested. The depth refers to the approximate penetration depth of the total coating thickness and is measured from the cross-section using SEM

Binder/solvent	Method	Pattern	Abbreviation	Indentation [μm]	Spacing [μm]	Depth
PVDF/water	Laser structured	Large lines	Laser-LL	21–42	200	100%
	Steel blade	Very large lines	BladePerf-VLL	30	450	50%
Lignin/water	Ceramic blade	Large lines	BladePerf-LL	10	200	50%
	Silicon wafer	Small lines	SL	20	100	30%
		Large lines	LL	20	200	30%
		Small pits	SP	60	150	40%
		Large pits	LP	100	150	50%

2.3.1 Laser structuring. Laser structuring was conducted on pre-made Targray cathodes (14.5 mg cm^{-2}) and in-house fabricated cathodes (4.7 mg cm^{-2}) after calendering. The in-house fabricated casts were calendered using an Electric Hot Rolling Press (MSKHRP01, MTI Corp.) T 22 °C and cut into 1.5 cm diameter discs. The structured electrode sheets were stored in an argon atmosphere but were eventually exposed to air during perforation.

Ultrashort-pulsed mid-infrared laser from ATLA Lasers AS operating around 2.1 μm was used as a structuring tool.[68,69] Laser emission was focused on the cathode surface by 11 mm focal distance aspheric lens antireflection coated at the laser operation wavelength. The movements of the cathode against the laser beam were carried out by the three-axis air-bearing translation stage, ensuring excellent positioning speed, precision, and repeatability. The combination of high scanning speed (0.4 m s^{-1}) and sufficiently high laser pulse repetition rate (20 kHz) ensured single-pulse laser processing-configuration when every next laser pulse does not overlap with the region of the cathode affected by the previous laser pulse. In combination with few-picosecond laser pulse duration, it allowed for minimized heat accumulation in the material affected by laser light and thus ensuring "cold" laser processing, in contrast with, for example, nanosecond laser processing, where the material volume is heated and melted by the laser light.

Laser structuring was done as a pattern of parallel 20 μm-wide lines located at a distance of 200 μm from each other. Since the single-pulse processing allows the removal of only a few micrometers of cathode material at once, to ensure the sufficient depth of the perforated lines laser beam was scanned 16 times over each line. The laser pulse energy was limited at the level of 20–40 μJ to avoid plasma formation in the focal region.

2.3.2 Structuring by compression. For the PVDF/NMP-based cathodes structured using the steel blades, the slurry was coated onto pre-cut titanium foil discs (134 μm thick, and 1.5 mm diameter), which served as the current collector. The structuring tool (10 blades) was pressed manually three separate times over the dried electrode surface to ensure complete surface structuring, and excess slurry residuals were removed with ethanol from underneath the Ti foil. This resulted in a line structure where no active material was removed since the blades only compressed the material.

Fig. 3a shows the steel blade structuring tool, with separator disks between the blades. The width of the blade-tip was 20 μm. The blades increased in width towards the blade's connection points, where the maximum width of 490 μm was reached. The thickness of the separator disks was 100 μm, resulting in a very large line spacing (∼450 μm).

The ceramic blade structuring tool was used on lignin/water-based cathodes Fig. 3b. It was placed on the half-dried electrode cast and removed when the electrode coating was completely dry. It consisted of 100 blades with a thickness of 200 μm ceramic blades mounted next to each other, resulting in the large line spacing (LL).

The third compressive structuring tool was a silicon wafer with four different structures, as illustrated in Fig. 3c. A pattern was exposed by using a mask-less aligner (MLA150, Heidelberg Instruments) in ma-N 440 on a 4-inch silicon wafer. By using lift-off, the pattern was transferred to a 250 nm Cr layer functioning as a hard mask for subsequent processing. The silicon wafer was structured by selective removal of silicon defined by the Cr pattern using the inductively coupled plasma reactive ion etching (ICP-RIE) technique. Four different structures were created: large lines (LL) and small lines (SL) with 100 and 200 μm spacing between the indentations, respectively. The indentation width of both lines was 30 μm. Additionally, the wafer had pit structures (P), which were used to create holes in the cathode surface. The spacing between the pits was 150 μm. The
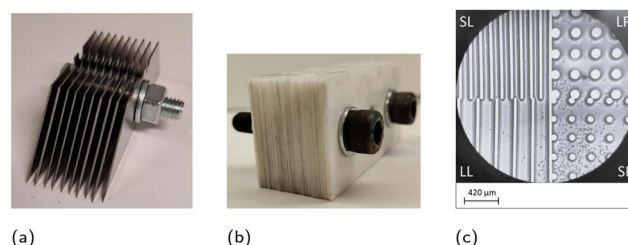

(a) (b) (c)

Fig. 3 The three types of structuring tools used to compress the electrode surface mechanically. (a) Steel blade creating very large lines (BladePerf-VLL) with 450 μm spacing. (b) Ceramic blade creating large lines (BladePerf-LL) with 200 μm spacing. (c) Silicon wafer creating lines (L) with 200 or 100 μm spacing, and pits (P) with a radius of 60 or 100 μm, and 150 μm spacing.

This journal is © The Royal Society of Chemistry 2023

J. Mater. Chem. A, 2023, **11**, 6483–6502 | **6487**

small pits (SP) and large pits (LP) had diameters of 30 μm and 50 μm, respectively. Each structure had a depth of 100 μm.

2.4 Cell assembly

All cathodes underwent post-drying in a vacuum for a minimum of 5 hours at 120 °C after perforation and before cell assembly to remove moisture and were then transferred into a glove box (MBRAUN) with an argon atmosphere ($H_2O < 0.1$ ppm and $O_2 < 0.1$ ppm) for cell assembly. The electrode discs were assembled into coin cells (CR2032 316 stainless steel, MTI Corp.) with steel space fillers and a spring in an argon atmosphere, using a pre-cut Li-metal disc (TMAX) as the anode and a semi-permeable polyethylene separator (Celgard 2320). The crimper machine (pneumatic crimper, MSK-PN110-S, MTI) was used with a pressure of 90 psi for 3 seconds.

2.5 Galvanostatic measurement

The coin-cells were tested electrochemically through galvanostatic cycling (Lanhe CT2001A potentiostat and a Biologic BCS-805) at 25 °C between 3.0 V to 4.3 V at varying current densities (*i.e.* C-rates), where 1C = 160 mA g^{-1}. All measured potentials were relative to Li/Li$^+$ since the anode was Li-metal.

Three different programs were used to test the coin cells, as demonstrated in Table 2. Form contained the first three formation cycles at 0.1C and ensured an effective SEI formation. Soak had a final cycle of 0.1C, followed by 15 cycles at 0.2C to reveal proper cycling stability.[30] The Rate test was conducted after, to investigate the cell performance at high discharging C-rates (2.5C and/or 5C), before ending the last 5 cycles at low C-rates (0.1C, 0.2C or 0.3C) to investigate the recovery and irreversible side reactions. For all C-rates up to 0.5C, the cells were charged and discharged at the same currents, but for all C-rates above 0.5C, the cells were charged at low C-rates (0.5C).

The post-mortem analysis was conducted on the electrodes after the cycling programs described in Table 2. The fully discharged cells were disassembled in an argon-filled glove box, and the cathodes were washed in DMC and soaked for 10 min, vacuum-dried at 120 °C for 5 hours, and stored in an argon atmosphere before being analyzed in SEM/EDS.

2.6 SEM/EDS analysis

Structural and elemental analysis was conducted using field emission scanning electron microscopy (FESEM) on a Zeiss Ultra 55 with an Everhart-Thornley secondary electron detector operating in secondary electron mode. This was used to characterize randomly selected cathode areas before and after cell assembly, and post-mortem. The structure dimensions of the cathode surfaces were measured from the SEM images, and ImageJ (Version 1.53) was used for data analysis. The working distance varied between 10 and 20 mm, and the accelerating voltage was 10 kV.

Energy dispersive X-ray spectroscopy (EDS) was conducted on the same apparatus with a Bruker XFlash EDS detector at a working distance of 10 mm and an accelerating voltage of 15 kV. Bruker ESPRIT (Version 1.9) was used for elemental analysis. The particles were scanned with a point scan at three different locations (magnification: 5000×), and the electrode surface was scanned using elemental mapping at three different areas with three different magnifications at each location (magnification: 100×, 200×, and 500×). The scanning time was 10 minutes.

2.7 Cyclic voltammetry

Cyclic voltammetry (CV) was performed using a Biologic BCS-805 device on coin cells with plain Ti and Al foil to reveal the voltage stability window of these current collectors. The cells were swept at voltages between 2.8 and 4.5 *vs.* Li/Li$^+$ with a sweep rate of 1 mV s^{-1} at 25 °C.

3 Results and discussion

Firstly, laser and mechanical structuring methods are tested on PVDF/NMP-based cathodes of low and medium mass loadings to reveal their robustness and scalability. The preferable method will be employed to structure lignin/water-based cathodes.

3.1 The PVDF/NMP cathode

The rate capability of unstructured and blade-structured PVDF/NMP cathodes with different mass loading, thickness, and porosity are investigated in this section and presented in Fig. 4. Thereafter, laser structuring and mechanical blade structuring are tested on the cathodes with medium mass loading (M-ML = 12.6–13.5 mg cm^{-2}). The method's electrochemical performance and structural integrity will be discussed.

3.1.1 Blade structuring. Fig. 4 shows the rate capability as a function of the PVDF/NMP-based cathode's mass loading, porosity, and surface structuring. The capacity retention during the third formation cycle (0.1C) and the capacity retention (%) at 2.5C are shown in Table S10.†

The capacity varies between 138.6–160.4 mA h g^{-1} after three formation cycles at 0.1C. No obvious trends were causing this variation, therefore only capacity retention is considered in this paper. No significant discrepancies are found in the capacity retention (CR) for the cathodes when cycled at a low discharge current density of 0.2C. At discharge currents from 0.5C and above, the capacity retention is a function of the electrode coating's porosity and mass loading.

Table 2 The lignin/water samples were subsequently cycled through the three programs; formation (form), soaking (soak), and rate-testing (rate), ending at a total of 54 cycles. The PVDF/NMP-based cathodes did not have a soaking step and had a total of 35 or 45 cycles. The blade structure had a max C-rate of 2.5 instead of 5* and ended at 0.2C instead of 0.1C. The laser-structured PVDF/NMP cathodes ended the rate test at 0.3C

Program name	0.1C	0.2C	0.5C	1C	2C	2.5C	3C*	5C*	Cycles
Form	3	—	—	—	—	—	—	—	3
Soak	1	15	—	—	—	—	—	—	16
Rate	5	—	5	5	5	5	5	5	35

6488 | *J. Mater. Chem. A*, 2023, **11**, 6483–6502

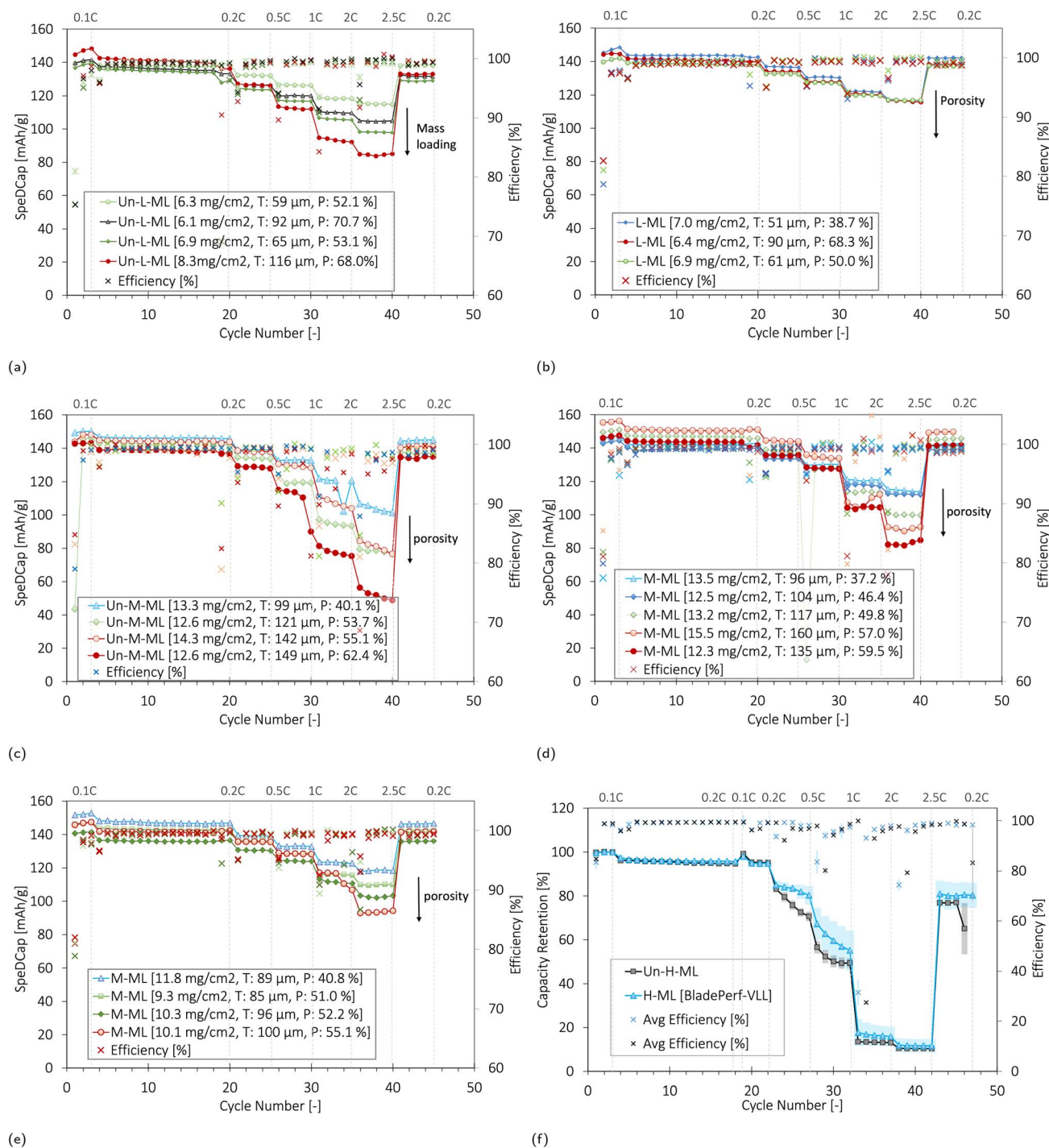This journal is © The Royal Society of Chemistry 2023

Fig. 4 Specific discharge capacity (SpeDCap, mA h g⁻¹) or rate capability (%) and coulombic efficiency of cathodes fabricated using PVDF/NMP as binder/solvent. The cathodes' mass loading (ML) were low (L), medium (M) in (a and b) and (c–e), respectively. The porosity (P) and thickness (T) varied, where P: 30–40% (blue), 40–55% (green), 55–70% (red), >70% (black). Unless specified with unstructured (Un), the cathodes were structured with very large lines using steel blades (BladePerf-VLL). The H-ML cathode's in (f) varied between 18.1–22.6 mg cm⁻² (Un-H-ML) and 19.5–21.3 mg cm⁻² (H-ML-[BladePerf-VLL]) with a porosity of 35–50.1%.

There are some clear trends demonstrated in Table S10†: (1) the capacity retention decreases with a higher mass loading, (2) the capacity retention is higher for the low-porosity cathodes, and (3) after surface structuring, the cathodes with the VLL pattern using steel blades (BladePerf-VLL), the rate capability increases.

The capacity retention is highest for the unstructured and structured cathodes that are calendered down to low porosities (37–50%), and steadily drops as the porosity increases to 70%.

This journal is © The Royal Society of Chemistry 2023

J. Mater. Chem. A, 2023, 11, 6483–6502 | **6489**

The capacity retention is; therefore, heavily dependent on the electronic conductivity within the coated layer for the PVDF/NMP-based cathodes.

Fig. 4 reveals that as the porosity and thickness decrease upon calendering, the rate capability generally increases due to improved electronic conductivity within the cathode coating. This trend is seen for the unstructured low mass loading (L-ML) cathodes (Fig. 4a), the cathodes with medium mass loading (M-ML) with VLL surface structures (Fig. 4d and e), and without surface structures (Fig. 4c).

High porosity is necessary to provide proper diffusion pathways for the Li$^+$, but it must be kept low enough to maintain a connection between the particles within the coating. The pores determine the ionic and electrical conductivity within the electrode coating and are often regulated through calendering. At an average porosity of ~37–40%, the ionic and electronic conductivity within the PVDF/NMP-based cathode coating is optimal.

An exception to this trend are the cathodes with low mass loading (L-ML = 6.4–7.0 mg cm^{-2}) that were structured with large lines using steel blades (BladePerf-VLL) in Fig. 4a. Each obtained high capacity retention irrespective of the porosity.

When comparing the high porosity (70.7% and 68.3%) unstructured and structured L-ML cathodes of similar thickness (90–92 μm) in Fig. 4a and b, the capacity retention increases from 74.2% to 80.4%, respectively. The compressed areas introduced by the VLL structures presumably allow for higher electronic conductivity. The mechanically structured VLL pattern increases not only the ionic conductivity but also the electronic conductivity of the L-ML cathodes.

The unstructured cathodes with medium mass loading (M-ML: 12.6–14.4 mg cm^{-2}) in Fig. 4c obtain a relatively low rate capability compared to the unstructured with low mass loading (L-MT = 6.1–8.3 mg cm^{-2}) in Fig. 4a.

The porosity reduction is increasingly important when going from a low (L-ML) to medium (M-ML) mass loading as the capacity retention improved with < 7.8% and 19% after calendering to ~40% porosity, respectively. The M-ML cathodes in Fig. 4c are pressed down from 149 μm to 99 μm, whereas the L-MT in Fig. 4a is pressed down from 116 μm to 66 μm. The high cathode thickness for the M-ML cathodes elongates the Li$^+$-diffusion path and facilitates polarization at elevated C-rates, eventually resulting in a lower CR.

Surface structuring the PVDF/NMP-based cathodes with a BladePerf-VLL pattern increases the cathode's capacity retention from C-rates > 0.5C. For example, the unstructured cathode with L-ML = 6.9 mg cm^{-2} with a porosity of 53.1% retains 70.7% of its initial discharge capacity at 2.5C, whereas the structured cathode with equal mass loading (6.9 mg cm^{-2}) and porosity (50%) retained 82.0% of its capacity at 0.1C.

Interestingly, the M-ML cathodes with high thickness and porosity (red, Fig. 4c) showed the most considerable improvement in capacity retention after structuring red, Fig. 4d. This further confirms the hypothesis discussed above for L-ML; the structures induce compressed areas in the cathode, which increases the electrical conductivity while the Li$^+$-diffusion length associated with the cathode thickness is reduced.

The average rate capability of three unstructured and structured high mass loading (H-ML = 18.1–22.6 mg cm^{-2}, *P*: 35–50.1%) cathodes is plotted in Fig. 4f. Here, there is little variation in the rate capability compared to those with lower mass loading (M-ML and L-ML). Still, the VLL structures increased the rate capability of H-ML from 0.2–2C. At 2.5C, the structures were no longer sufficient to reduce the polarization for the thick electrodes. Also, very few Un-H-ML cathodes retained their full capacity after the rate test. The structures improve the wetting and homogeneity of the reactions across the coating, which cause less structural damage during cycling.

These cathodes used a pre-cut Ti foil (134 μm thickness) as a current collector instead of the Al or C–Al foil as the steel blade damaged the Al foil. The CV in Fig. S12† revealed no additional reduction or oxidation peaks within the potential window used for these coin cells (3.0–4.3 V) when comparing the Ti with an Al-foil. Elaboration on this analysis is discussed in Subsection 5.1 (Fig. S10b†).[70–72]

In summary, the mechanically structured calendered PVDF/NMP cathodes obtain a higher rate capability than the uncalendered, unstructured cathodes due to the combination of high electronic and ionic conductivity. The VLLs create Li$^+$ diffusion pathways that improve the cathode's ionic conductivity.[64] A porosity of ~40% provides a sufficient ionic, and electronic conductivity.[40]

The rate capability depends not only on ionic diffusion but also on a sufficient electronic connection between the electrode particles. The results corroborate the important aspect of inducing structures on the electrode surface rather than maintaining a high bulk porosity by avoiding a high calendering pressure.

These findings illuminate the importance of revealing the electrode's porosity and thickness, in addition to its mass loading, when examining the rate capability.[38] Therefore, the porosity and thickness should be specified rather than the mass loading when discussing the rate capability of electrodes.

3.1.2 Laser structuring. The PVDF/NMP cathodes with a medium mass loading (M-ML = 14.5 mg cm^{-2}, pre-made from Targray) and low porosity (23.9%) are line structured with a subtracting laser ablation method. The unstructured and structured cathodes showed similar initial capacities of 156.8–160.6 mA h g^{-1} and 149.0–157.3 mA h g^{-1}, respectively.

The average rate capability of four unstructured and laser-structured cathodes are presented in Fig. 5. No differences are detected in the capacity at low C-rates, but the laser structures improve the rate capability at high discharge currents (≥2C). The laser-structured lines increase the average porosity and improve the electrolyte penetration by decreasing the diffusion path for Li$^+$. Since the bulk porosity remains low (29.5%), high electric conductivity is maintained.

Laser structuring is also conducted on a low mass loading cathode fabricated in-house (L-ML: 4.7 mg cm^{-2}) to reveal how the packing density (*i.e.* thickness and porosity) affects the structuring quality.

Table 3 shows that the Targray cathode with a medium mass loading (M-ML = 14.5 mg cm^{-2}) and low porosity (23.8%) experiences a weight reduction (mg) of 15.5% during laser

6490 | *J. Mater. Chem. A*, 2023, **11**, 6483–6502

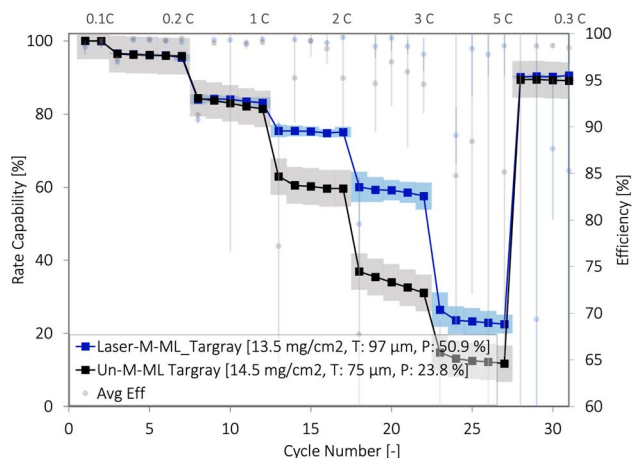This journal is © The Royal Society of Chemistry 2023

Fig. 5 Average rate capability and coulombic efficiency (%) of four unstructured and laser-structured PVDF/NMP-cathodes fabricated by Targray with medium mass loading (M-ML).

Table 3 Mass loading, porosity, coating thickness for unstructured (Un) and laser structured large lines (laser-LL) cathodes fabricated using PVDF/NMP as binder/solvent. The medium-thick (MT) electrodes originate from Targray, and the low-thickness (LT) electrodes were fabricated inhouse

	Targray (calendered)		Inhouse (uncalendered)	
Origin of electrode Sample	Un-MT	Laser-LL-MT	Un-LT	Laser-LL-LT
Mass loading [mg cm^{-2}]	14.5	13.5	4.7	3.3
Porosity	23.8	50.9	50.9	59.1
Thickness [μm]	75	97	38	32

structuring, whereas the in-house cathode with a low mass loading (L-ML = 4.7 mg cm^{-2}) and high porosity (50.9%) has a 29.9% weight reduction. This is because the amount of active material per unit volume is higher for a high-density electrode, and the line structure is limited by the laser beam's width. When considering the waste material, the subtracting laser method becomes increasingly cost-efficient for electrodes with higher thicknesses and porosities. The reduced mass of the electrodes is directly proportional to the capacity loss and varies with the size, shape, and pitch of the structured pattern. Optimizing these structure parameters, as well as using ultra-short laser processing, is necessary to enhance performance while reducing the waste electrode material for laser-structured electrodes.

The material loss causes an increase in the average porosity after laser structuring for both the uncalendered inhouse-cathodes and the calendered Targray-cathodes.

The laser treatment causes an increase in the average coating thickness for the calendered laser structured cathodes from Targray, while no such increase was observed for the uncalendared laser structured in-house fabricated cathodes or those structured mechanically (Table S8†). Hille *et al.*[55] suggested that the thickness increase for calendered laser-structured

electrodes was caused by a spring-back effect induced by the heat input from the laser radiation. The cathode coating presumably expanded abruptly upon the laser irradiation and released tension introduced into the electrode coating during the calendering process.[55]

The spring-back effect is seen after laser structuring; therefore, it increases the bulk porosity of the calendered Targray electrodes after structuring. The spring back effect increases the bulk porosity from 23.8% to 29.5% for the laser-structured cathode when using the new thickness (97 μm) in the porosity calculation.

3.2 Comparing structuring methods

The main differences between the laser structuring method and the mechanically structuring method are summarized in Table 4.

The capacity retention for unstructured, inhouse-fabricated PVDF/NMP cathodes with mass loading (M-ML = 13.3–13.5 mg cm^{-2}, 37.2–40.1% porosity) increases from 78 to 83% at 2C after being mechanically structured with the BladePerf-VLL pattern. The capacity retention for the Targray cathodes with similar mass loading (13.5 mg cm^{-2}) but lower bulk porosity (23.8–29.5%) increases from 60 to 75% at 2C after being structured with the laser-LL pattern.

Although the capacity retention is generally higher for the mechanically structured cells, the laser-structured lines induced a larger improvement (15%) than the mechanical method (5%). Thus, the Li$^+$ conduction pathways had a larger positive impact on the dense electrodes.

The overall higher rate performance for the PVDF/NMP-based cathode with porosities between 37.2–40.1% indicates that this porosity is preferred to provide sufficient electronic and ionic conductivity, whereas, at a lower porosity (23.8–29.5%), the ionic conductivity is compromised.

At a medium mass loading (M-ML = 13.3 mg cm^{-2}), a 40.1% bulk porosity is beneficial for an overall high rate performance compared to calendering it down to 23.8% and then increasing the average porosity by inducing pore channels into the electrode surface. However, dense cathodes obtain higher mechanical stability and are less prone to cracking and degradation during cycling, as discussed in the Section below.

3.2.1 Structural and chemical analysis. The laser-structured and mechanically structured PVDF/NMP-based cathodes were analyzed in SEM and EDS before and after cell assembly,

Table 4 Overview of findings for the laser structured and mechanically structuring methods

	Laser ablation	Mechanical compression
Residuals	Mn along lines	N/A
Thickness	Increase	Unchanged
Material loss	15–13%	None
Average porosity	Increase	Change in local pore size
Bulk porosity	Increase	Unchanged
Spring compression	Yes	Yes

and after the rate test (post-mortem) to reveal the micro-structural and chemical integrity of the cathode coatings.

The structure's dimensions measured using SEM are presented in Table 1. An important difference between mechanically structured and laser-structured cathodes is the depth of the indentations. While the laser structures reached 100% depth, mechanically structured patterns penetrated ∼ 30–50% of the cathode thickness, yielding an increased density of material beneath this area with lower porosity than the bulk (Fig. 2). Some of the excess material may also be displaced to the sides during the mechanical structuring, which can increase the density of small regions in between the perforations.[66]

The mechanical stability of the structures during cycling is strongly dependent on the initial bulk porosity of the cathode. The laser structures in the calendered dense Targray cathode with high mass loading (13.5 mg cm^{-2}, 23.8% bulk porosity) are constant throughout the rate test cycling (35 cycles), Fig. 6a. The cathode remains attached to the Al foil current collector throughout the disassembly of the cell, indicating strong adhesion to the Al. However, the uncalendered low-density fabricated cathode (50.9% bulk porosity) with low mass loading (3.3 mg cm^{-2}) reveals major structural changes after the same rate test, as illustrated in Fig. 6b. The structures are filled with particles in Fig. 6b. Furthermore, the adhesion to the Al foil is poor for these uncalendered cathodes, as the material detaches from the edge of the disc during cell disassembly.

The extensive structural degradation of structures imprinted into the uncalendered cathodes is caused by the high porosity and the extensive cracks present on the surface. Pores and cracks are usually removed during calendering (Fig. S11†) but weaken the mechanical stability of the coating as they create space for structural changes to occur during cycling.

Large cracks, in combination with the high bulk porosity of the low-density cathode, increase the free volume of which the particles can move within the cathode coating, making it prone to structural changes during cycling.

The same phenomenon is detected in the SEM analysis for the BladePerf-VLL structured PVDF/NMP-based cathode in
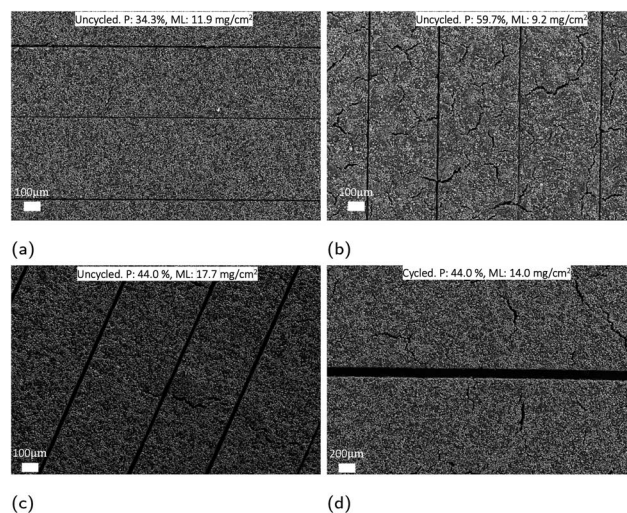

Fig. 7 SEM analysis of the PVDF/NMP-based NMC111 cathodes mechanically structured very large lines (BladePerf-VLL) by using a steel blade. The images show the surface of (a), (b), and (c) uncycled cathodes with different porosities and mass loadings, and (d) a cycled cathode.

Fig. 7. The low-density cathode (59.7% average porosity) in Fig. 7b has more extensive surface cracks relative to the calendered low-density cathode (34.3% average porosity) in Fig. 7a.

To summarize, the structured patterns remain unchanged during cycling when structuring calendered cathodes with a relatively high mass loading (M-ML) and low bulk porosity (23.8–44.4%) due to high mechanical stability.

3.2.2 Crimping. A structural change was found on the surface of the cathode after the cell assembly, as shown in Fig. 8. Compressive forces perpendicular to the electrode surface were induced during the coin cell crimping step. Evidence of high pressure under the spring is also found at the Li metal anode from the same uncycled crimped cell as the structures embossed a line pattern in the Li metal anode, ESI Fig. S5c.†
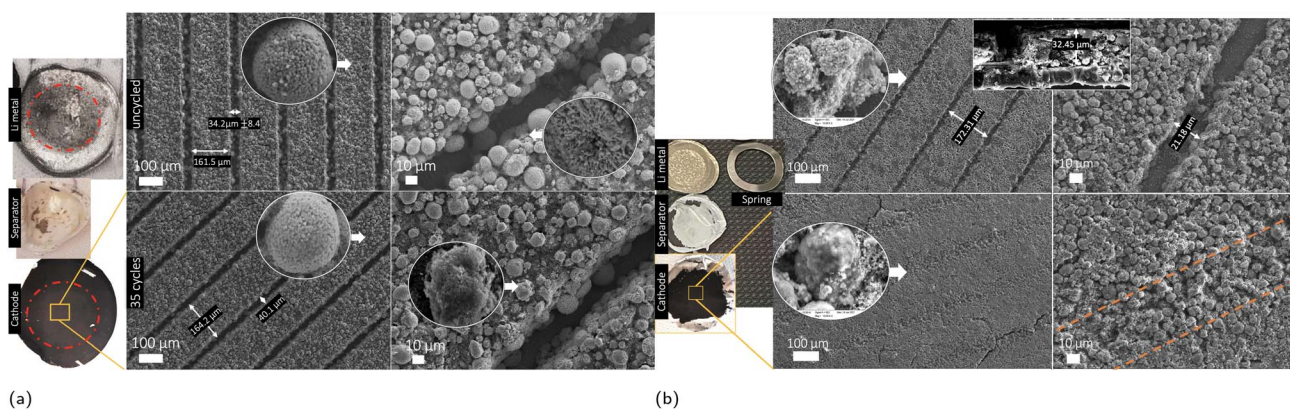

Fig. 6 SEM analysis of cathode sheets with large line (LL) laser structures, before (upper images) and after (lower images) a rate capability test of 35 cycles. (a) Targray (M-ML: 13.5 mg cm^{-2}) or (b) inhouse (L-ML: 3.3 mg cm^{-2}). The circular figures show a zoomed particle (at 10× the magnification of the right-sided images). All cells had an NMC111 : CB : binder ratio of 90 : 5 : 5 wt% and were cycled towards Li-metal in coin-cells with 1C = 160 mA g^{-1}.

6492 | *J. Mater. Chem. A*, 2023, **11**, 6483–6502

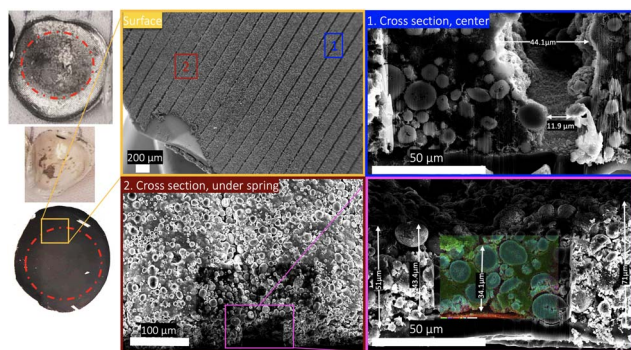This journal is © The Royal Society of Chemistry 2023

Fig. 8 Post mortem SEM analysis of the laser structured surface and cross-section of Targray electrode sheets. The structures in the center of the electrode disc (upper, yellow, and blue frames) and the compressed structures under the spring (lower, red frames).

The compressed structures may be avoided by carefully adjusting the crimping pressure during cell assembly or utilizing other cell formats than coin cells for structured electrodes. Few studies have investigated this phenomenon, and the crimping pressure's impact on cycling performance should be studied further if the commercialization of structured coin cells is of interest. Since all electrodes showed structural damage due to the crimping pressure, the effect of compressed structures on the cycling performance was neglected in this study.

3.2.3 Surface residuals. Beyond the general geometry of the patterned channels, it is important to understand the impact of residual formation that may arise from laser ablation if the laser pulses are not optimized.

An SEM analysis of the particles on the laser-structured PVDF/NMP cathode's surface in Fig. 6 shows signs of composition and structural irregularities along the laser-ablated channels. Damaged NMC particles are detected along the laser-structured lines, revealing that the laser acts destructively on the NMC particles. This has also been reported earlier.[57] Neither of these findings is detected in the mechanically structured cathodes (Fig. S6†).

An EDS analysis is conducted on the surface of a laser-structured (Fig. S8†) and a mechanically structured (Fig. S9†) PVDF/NMP-based cathode surface. A significant presence of manganese (Mn) is detected along the laser-structured lines (Fig. S8a†) and in the filled laser-structured lines (Fig. S8b†). No excessive Mn is detected on the surface of the mechanically structured lines before or after cycling (Fig. S9†). Mn likely arises from the destructed NMC particles, as NMC particles[57,58] temporarily melt under fast pulsed laser exposure at ambient pressures. The same holds true for graphite anodes.[73,74] Furthermore, laser processing parameters like pulse duration, pulse repetition rate, and scanning speed also strongly affects the quality of laser-processed $LiFePO_4$ cathodes.[59] In general, short pulses, such as femtosecond and picosecond lasers demonstrate considerably better structuring quality.

Managang *et al.*[59] presented images of melted $LiFePO_4$ material; however, these results does not resemble our findings.

Additionally, the surface SEM analysis of the Al current collector used for the laser structured PVDF/NMP-based cathodes (Fig. S2†) reveals no sign of melting. This indicates that the heat accumulation in the short-pulse laser in this study was minimal. The laser used in this paper has a picosecond pulse duration, and by a proper choice of the scanning speed and pulse repetition rate, we ensured minimal heat accumulation.

However, even for short-pulse lasers, one has to balance the processing speed with an appropriate pulse repetition rate to avoid pulse overlap, local heat accumulation, and melting. No special measures have been implemented to avoid the deposition of the pieces of the laser-ablated material around the laser-processed lines. The surface residuals detected in SEM are presumably mainly caused by deposition rather than melting and may be reduced by properly evacuating the ablated material.

It should be mentioned that the laser-structured lines were initial experiments for this laser and that the laser-structuring instrument with ultra-short pulse duration offers a large potential for further optimization regarding the line precision and reduction of waste material, and ventilation for material deposition. Thus, waste material and residuals are expected to be reduced after efforts to improve the line precision, waste material, and processing efficiency.

The accuracy and repeatability of the line structures are improved for laser structuring compared to the mechanical structuring method. Thus, laser structuring with ultra-short pulses is preferred for large-scale production over mechanical structuring, if the processing can provide no residual formation and material losses. Secondly, the reduces investment costs considering processing tools as mechanical blades need to be replaced often, while the laser operates for more than 100 000 hours.

SEM analysis of the NMC particles at the Targray (M-ML) and inhouse cathode (L-ML) surfaces show an increasing residual formation towards the laser structured lines in Fig. S1.† The post-mortem analysis in Fig. S4† indicates that these residuals initiate the formation of a thicker cathode electrolyte interphase (CEI) layer during cycling. A thick CEI layer mainly consists of decomposition species from the electrolyte and is known to limit the intercalation of Li^+ into the NMC111 particles due to increased resistance.[75] This may explain the overall lower rate performance for the laser-structured cells (79% at 2C) compared to the mechanically structured cells (85% at 2C) with a similar thickness (97–99 μm), mass loading (M-ML = 13.5 mg cm^{-2}), and porosity (29.5% (laser) or 37.2% (mechanical)). However, a thin and stable CEI layer may also act as a passivizing layer which prevents the oxidative decomposition of the electrolyte and enhance the stability of the cathode/electrolyte interface.[76]

An EDS mapping is conducted on the NMC particles before and after cycling to detect any difference in the presence of phosphorous (P) or fluorine (F) from the PVDF binder or the electrolyte $LiPF_6$ salt.

The EDS analysis of uncycled cathodes shows no residuals of phosphorous (P), confirming that this element arises from the electrolyte decomposition (CEI layer) during cycling. There is a clear increase in fluorine (F) and P on all cathode surfaces

This journal is © The Royal Society of Chemistry 2023

J. Mater. Chem. A, 2023, **11**, 6483–6502 | **6493**

after cycling in Table S4,† which confirms the presence of a CEI surface layer formed by electrolyte decomposition.

To further quantify the chemical composition of the laser-patterned cathodes, three EDS point scans were conducted on the NMC particles and the CB/PVDF matrix. These scans were (1) on the structure edge, (2) near the edge (10 μm from the edge), and (3) at a maximum distance from the laser-ablated channels. ESI Table S3† sums up the EDS analysis for both the laser-structured cathode sheets with small structural changes (Targray) and large structural changes (inhouse) during cycling. Like the surface EDS surface scan, the particle scan confirms an increase in the Mn content on the surface of the laser-structured lines.

The image of the Li metal anode in Fig. 6 shows that extensive deposits are found in the center of the disc, where there was no spring. On the side of the discs, the pressure from the spring promotes deposition on the rough cathode surface rather than on the Li metal. Therefore, two places on the electrode discs are investigated in EDS; the center of the disc (low-pressure zone) and the area under the spring (high-compression zone). In the post-mortem EDS scans in Table S3,† more deposits of P and F are detected at the surface under the spring than at the center of the disc for the laser-structured Targray electrodes. The area closer to the laser-structured lines also has more residuals of F and P when compared to the area with maximum distance from these lines.

For the inhouse-fabricated cathodes with extensive structural changes, there was also a significant increase in the F concentration after cycling. However, unlike the Targray cathode sheet, the inhouse-fabricated cathode showed no local differences in the deposition of P over the cathode surface, because it undergoes large overall structural changes during cycling.

Here, the differences between the coulombic efficiencies (CE [%]) most likely reflect differences in the formation of a CEI, as the same electrolyte and counter electrode (lithium) are used. The CE is summed up in Table S5† for the unstructured, laser-structured, and mechanically blade-structured PVDF/NMP-based cathodes.

For the pre-made Targray electrode sheets (13.5 mg cm^{-2}), there were no significant differences in CE before (85.66 ± 1.14%) and after laser-structuring (86.13 ± 0.93%). However, the excessive structural changes detected for the laser structured inhouse-fabricated sheets (3.3 mg cm^{-2}) seen in SEM and from the particle analysis in Subsubsection 3.2.1 are recognized as a low CE (68.41 ± 2.69%) during the first cycle. After the fourth formation cycle at 0.1C, the CE was generally lower for the laser-structured cathodes, which indicates that the extra side reactions promoted by the residuals were somewhat detrimental to the initial reversible capacity.

No significant differences are detected for the CE in any of the formation cycles of unstructured (70.53 ± 12.38%) and mechanically structured cathodes (77.46 ± 7.46%) structured cathodes. The structure imposes negligible structural changes during the formation of these cathodes. The overall lower CE is caused by their larger porosity, which took a long time to activate the entire cathode.

To conclude, the structuring method with the highest potential for large-scale employment was the mechanical structuring method using compression forces. This will therefore be employed to structure lignin/water-based cathodes.

3.3 The lignin/water cathodes

The structure analysis and rate performance of unstructured and mechanically structured lignin/water-fabricated cathodes with different porosity and mass loading will be presented in this Section.

3.3.1 Calendering. Fig. 9a shows the effect of calendering on the rate capability for unstructured lignin/water-based cathodes with medium mass loading (M-ML = 12.3–14.1 mg cm^{-2}). The cathode's thicknesses are pressed down from 147 μm to 99 μm and 78 μm by reducing the porosity from 57.1% to 41.3% and 29.5%, respectively.

Generally, the rate capability is low for the uncalendered and calendered M-ML cathodes. At a porosity of 29.5%, there were no proper pathways for Li$^+$-intercalation, whereas at the thickness of 147 μm the Li$^+$-diffusion pathway was too long and the active NMC111 particles done have time to participate in the reaction. Additionally, the electronic conductivity and particle connection are low at a 57.1% porosity when the carbon/matrix is low (90 : 5 : 5 NMC111 : CB : lignin). The uncalendered lignin cathode does not restore its full capacity at 0.2C after the rate test, which indicates a loss of active material. The calendering is therefore needed to provide a mechanically strong coating.

The low-porosity electrode (28.5%) is compared to a structured cathode with similar porosity (29.5%) and mass loading (M-ML = 11.6–12.3 mg cm^{-2}) in Fig. 9b. The structuring improves the rate performance and confirms that the ionic pathways in the electrode limit the rate capability for these cathodes with M-ML and low porosity.

The Li$^+$-diffusion limitation is further confirmed when looking at the lignin/water-cathode with low mass loading (L-ML = 3.5 mg cm^{-2}), low thickness (28 μm) and medium porosity (44.4%) in Fig. 14c presented in Subsection 3.4. Although this L-ML cathode has the same porosity (41.3%) as the M-ML cathode in Fig. 9a the low mass loading cathode provides excellent cyclability at high rates with a specific capacity of 95 mA h g^{-1} at 5C.

Like for the well-reported PVDF/NMP cathodes, the rate capability for the lignin/water-based cathodes is greatly determined by the mass loading, porosity, and thickness of the cathode due to a restricted Li$^+$-diffusion path.

3.3.2 Mechanical structuring. For the lignin/water-based cathodes, the effect of mechanical structuring was tested using two different structuring tools; a silicon wafer (SP, LP, LL, SL) or ceramic blades (BladePerf-LL). Four groups of cathodes were fabricated with similar porosity (39–50%). Each group and the corresponding thickness, porosity, and mass loading produced are presented in Table 5.

Table 6 summarizes the discharge capacity from the first and fourth cycles. The specific discharge capacity of the first formation cycle was low with large variations (124.8–157.9 mA h g^{-1}) but increased and stabilized after the fourth cycle (139.8–

6494 | *J. Mater. Chem. A*, 2023, **11**, 6483–6502

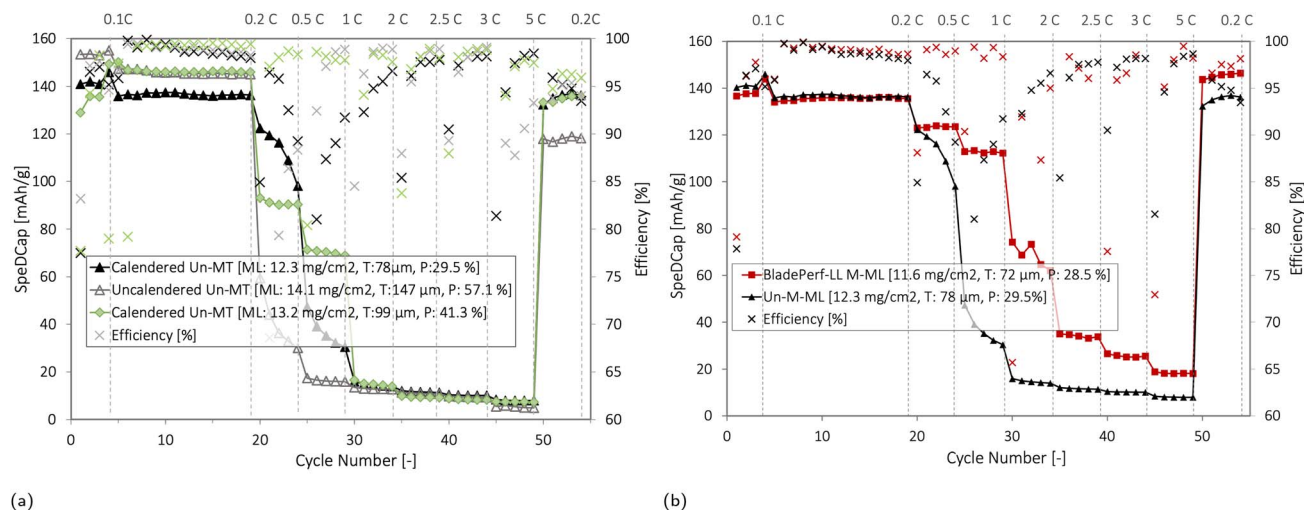This journal is © The Royal Society of Chemistry 2023

Fig. 9 The specific discharge capacity and coulombic efficiency (%) at different C-rates for lignin/water-based cathodes with medium mass loading (M-ML = 11.6–13.2 mg cm^{-2}). (a) Compares calendered and uncalendered unstructured (Un) cathodes, and (b) shows how structuring (LL) improves the rate capability of calendered cathodes with low porosity (P = 28.5–29.5%).

Table 5 The lignin/water cathodes have been grouped according to a low (L) medium (M), high (H), and ultra-high (U) coating thickness (T). The actual thickness and mass loadings (ML) are also shown. The porosities (P) were constant at $\approx 39 - 50\%$

Abbr.	T [μm]	ML [mg cm^{-2}]	Actual T [μm]	Actual P [%]
LT	≈ 50	6.6 ± 1.9	53 ± 16	44.0 ± 2.2
MT	≈ 100	12.9 ± 1.2	96 ± 9	39.6 ± 6.9
HT	≈ 150	18.9 ± 2.8	146 ± 13	42.2 ± 7.5
UT	≈ 200	26.9 ± 2.5	205 ± 15	41.2 ± 5.6

162.5 mA h g^{-1}). This was likely due to the poor electrolyte wetting associated with lignin, and the formation of SEI and CEI layers during the first cycles. Since they stabilize in the fourth formation cycle, the following rate capability plots are normalized as a function of this cycle, and the three first formation cycles at 0.1C are not accounted for.

Interestingly, there is an increasing trend in a higher initial capacity for lignin/water cathodes with higher thicknesses. More material may take part in the reactions in the first formation cycles for the thick electrodes compared with the

Table 6 Overview of the lignin-based cathodes, with the number of cathodes in each group, and the ranges in thickness, porosity, and the specific discharge capacity (SpeDCap) after the 1st and 4th cycle

Structure	Sample	Thickness [μm]	Porosity [%]	SpeDCap [mAh/g]	
				Cycle 1	Cycle 4
Unstructured	Un-LT	31–56	42.6–46.7	124.8–130.5	142.5–146.0
	Un-MT	78	29.5	140.4	146.0
	Un-HT	151–158	44.3–55.0	148.0–154.7	150.1-152.9-157.9
	Un-UT	181–209	51.7–57.2	156.7–157.9	158.0–161.1
BladePerf-LL	Perf-LT	62–71	23.6–51.6	126.5–140.8	127.3–141.7
	Perf-LL-MT	85–100	39.2–49.7	138.9–151.7	139.8–154.8
	Perf-LL-HT	147–157	57.1–68.4	152.5–153.4	155.0–157.1
Small lines	SL-LT	68	47.1	139.6	151.4
	SL-MT	100–115	35.9–51.1	128.9–141.7	141.3–143.0
	SL-HT	160–165	34.1–41.6	152.3–157.3	157.2-159.4-162.9
	SL-UT	177–226	38.6–40.7	149.2–155.3	156.4–156.3
Large lines	LL-T	60–72	28.0–42.4	133.9–136.7	144.0–144.5
	LL-MT	100–107	36.7–45.5	139.3–142.0	144.2–144.5
	LL-HT	123–163	53.4–59.8	129.6–134.5	141.8-148.8-155.8
	LL-UT	197–210	33.2–36.2	157.0–157.5	149.2–155.8
Small pits	SP-MT	98–117	45.4–50.6	136.9–152.1	143.4–157.1
	SP-HT	136–142	46.2–57.5	138.1–143.7	139.9–145.7
	SP-UT	181–202	36.6–41.0	152.5–157.3	160.0–162.5
Large pits	LP-MT	99–104	37.5–40.5	131.7–135.7	142.7–147.1
	LP-HT	146	30.3	149.8	150.3
	LP-UT	210	41.0	157.1	160.0

This journal is © The Royal Society of Chemistry 2023

J. Mater. Chem. A, 2023, **11**, 6483–6502 | **6495**

cathodes of lower thickness. Another reason contributing to the high capacity for the cells with higher mass loading may be the higher loss of active material during coin cell assembly for thicker coatings. Since coin cell assembly takes place after the weighing, the presence of active NMC111 particles is likely less than what was used to calculate the mA h g^{-1}, resulting in a higher capacity for cells with a larger loss of active material. The cathode cutting induced mechanically weak areas on the edge of the lignin/water-based cathodes.[30]

Fig. 10 shows the rate capability of lignin/water-based cathodes with medium thickness (MT) and compares the well-performing unstructured cathode with cathodes of different structure patterns (lines and pits) and structure-dimensions (small, large or very large spacing between the structures).

The plots highlight an important property of a well-functioning cathode; the initial capacity is recovered after the rate test when the current is reduced to 0.1C (or 0.2C for the PVDF cathodes). This indicates that no extensive degradation or parasitic reactions occur during cycling at high current densities. The capacity is recovered for both the PVDF/NMP-fabricated and the lignin/water-fabricated cathodes; meaning, the lignin binder offers a high mechanical and chemical stability for cathodes with a medium mass loading. As reported earlier,[9] lignin is one of the binders with the strongest binding abilities to carbon and is expected to induce high mechanical stability.

The capacity retention was higher from C-rates >0.5C for all structured cathodes, except those with large pits (LP). The LP cathodes failed due to difficulties in fabricating mechanically stable structures without cracks, as discussed below (Subsubsection 3.3.3).

The structured M-ML in Fig. 10 were plotted compared to a low porosity unstructured M-ML cathode, to show the rate capability for a cathode with proper ionic conductivity relative to a cathode with proper electronic conductivity. It is clear that for these lignin/water cathodes with low thickness, the calendering decreases the rate performance without improving the ionic conductivity.

The rate capability becomes increasingly dependent on the bulk porosity and calendering if the thickness is >78 μm, as the length of the Li$^+$-diffusion increases. An earlier report also showed that the calendering of low mass loading (7.4 mg cm^{-2}) lignin/water-based cathodes was beneficial at thickness >76 μm for 80 : 11 : 9 cathodes, as the Li$^+$-transport is limited in thick electrodes.[30] Below this thickness, the calendering restricted the ionic conductivity without improving the electronic network, and the rate performance decreased upon calendering.

A current of 0.5C was already too high for full utilization of the NMC cathode, before reaching the cutoff voltage. At very high currents (5C), only a slight increase was detected in the capacity for line-structured cathodes. This was similar to recent findings for structured 100 μm thick aqueous processed NMC622 cathodes, which obtained zero capacity at 5C.[57] The ceramic blade structured cathode (BladePerf-LL) in Fig. 10a shows the highest rate capability for all the lignin/water cathodes with a medium thickness.

The rate capability of unstructured and mechanically structured lignin/water-fabricated cathodes with four classes of mass loadings and thicknesses (low (LT), medium (MT), high (HT), and ultra-thick (UT)) presented in Table 5 and similar porosities are presented in Fig. 11. Each graph shows a different structuring pattern (line and pit structures) or dimensions (small or large spacing between the structures). For all these unstructured and structured cathodes, the rate capability decreased as the cathode thickness increased when current densities reached >0.2C. One exception was the unstructured electrode with the exceptional low porosity of 28.5% in Fig. 11a, due to Li$^+$-diffusion limitations, as discussed above in Fig. 9a.

Generally, the BladePerf-LL structures, and the SL, LL, and SP patterns created with a silicon wafer increased the cathode's rate capability for all coating thicknesses with similar porosity, except for those with high (HT) and ultra-high (UT) thicknesses. Common for the ultra-thick (200 μm) lignin/water-based cathodes (Un-UT1, SL-UT2, LL-UT2, SP-UT2, or LP-UT1) is that they failed to restore their full capacity when reaching 0.1C after the rate test. Thus, lignin/water-based cathodes with 200 μm thickness resulted in unstable cathode coatings, which are susceptible to degradation during cycling.
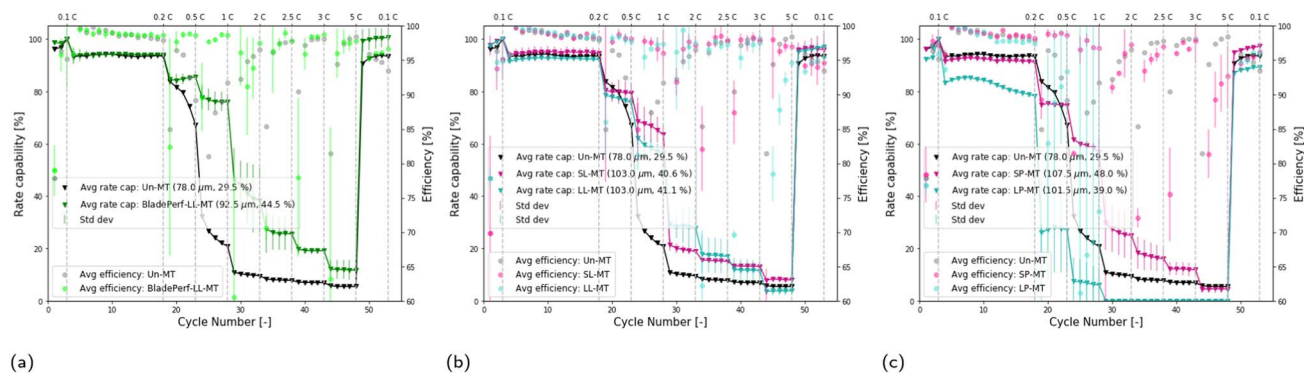

(a)   (b)   (c)

Fig. 10 Rate capability of structured lignin/water based cathodes coatings with a medium mass loading (Un-MT: 12.3 mg cm^{-2}, Blade-Perf_VLL: 10 mg cm^{-2}, SL-MT: 13.6 mg cm^{-2}, LL-MT: 14.1 mg cm^{-2}, SP-MT: 12.0 mg cm^{-2}, LP-MT: 13.9 mg cm^{-2}). The cathode surfaces were (a) line structured using ceramic blade blades (BladePerf-LL), or structured using a silicon wafer creating (b) large lines (LL) or small lines (SL), and (c) small pit (SP) or large pits (LP). Unstructured reference samples (Un) with low porosity (29.5%) are shown in black to illustrate the limitations in ionic conductivity when creating proper electronic conduction.
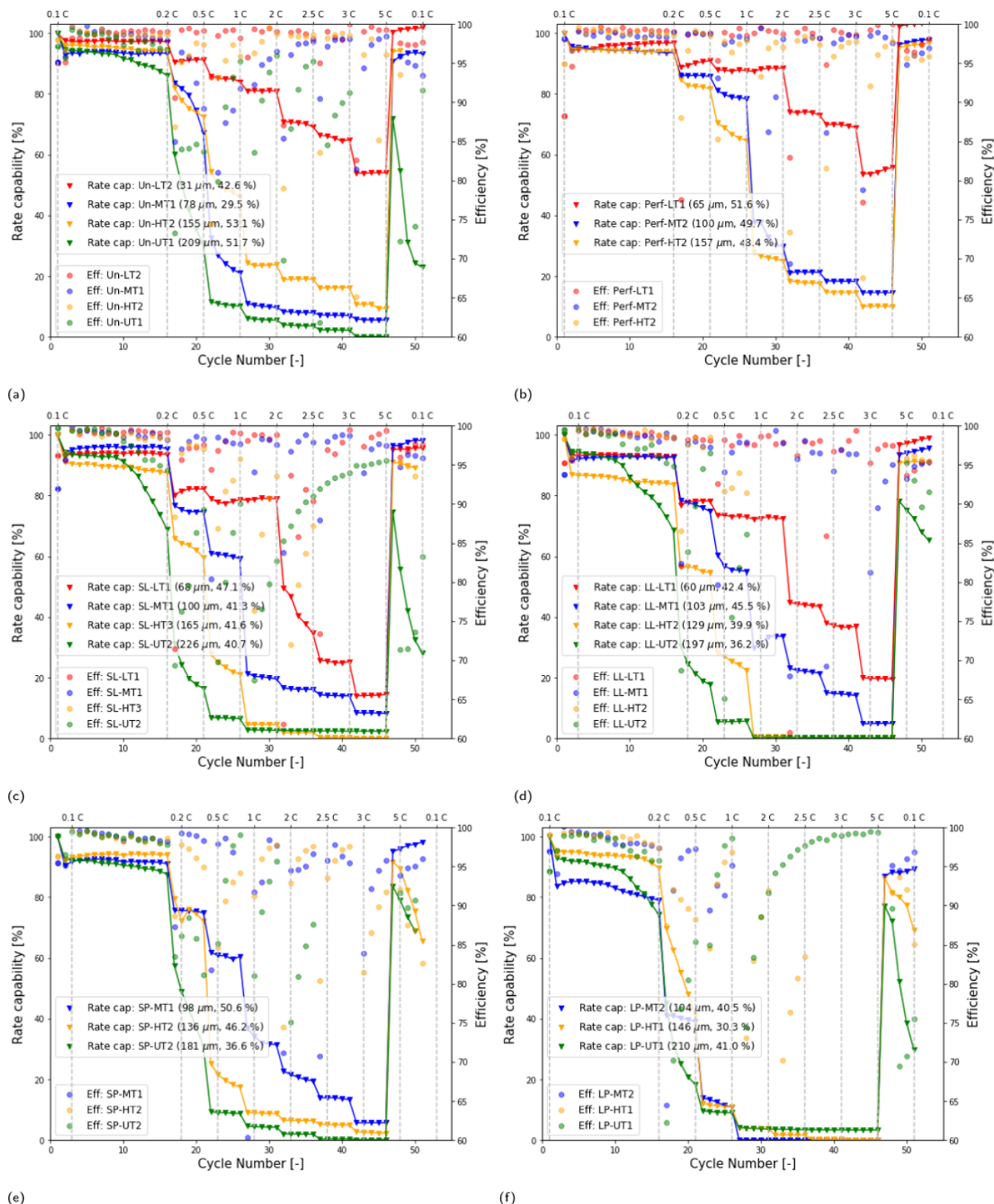
6496 | *J. Mater. Chem. A*, 2023, **11**, 6483–6502

This journal is © The Royal Society of Chemistry 2023

Fig. 11 Rate capability and coulombic efficiency of cathodes fabricated using lignin/water as binder/solvent with medium (M), high (H), and ultra-high (U) coating thicknesses (T) as defined in Table 5. The corresponding mass loading increases with the coating thickness as the porosity remains constant. (a) Unstructured (Un), (b) structured with ceramic blades creating large lines (BladePerf–LL), or structured with a silicon wafer creating (c) small lines (SL), (d) large lines (LL), (e) small pits (SL), and (f) large pits (LP).

This journal is © The Royal Society of Chemistry 2023

J. Mater. Chem. A, 2023, **11**, 6483–6502 | **6497**

Interestingly, for the cathodes with a high thickness (HT) of 150 μm, the irreversible capacity loss caused by mechanical degradation is no longer detected, except for those structured with pits (SP and LP). Similar findings are reported earlier for the aqueous processed NMC622 cathodes,[26] and for PVDF/NMP-based NMC622 when reaching a thickness of 250 μm.[63] This was also the case for the PVDF/NMP cathodes of high mass loading (18–22 mg cm^{-2}) reported above in Fig. 4f in Subsubsection 3.1.1.

Upon cycling, the active material suffers from a volume expansion and contraction during Li$^+$-intercalation and deintercalation. The volume change can induce and accumulate severe strain, which propagates as increased internal stress in the thick electrodes.[77] Especially at high C-rates above 1C, the rapid volume change will lead to crack formation or a fracture in the cathode laminate. Those cracks can cause particle isolation which results in capacity losses.[63] Others[34,35] have reported that low mechanical stability is common for aqueous fabricated cathodes as more extensive crack formation occurs in the electrode coating during solvent evaporation.

Another factor that may cause a decreasing rate capability is the side reactions, such as electrolyte oxidation with metallic Li. This promotes the growth of the resistive surface layer and increases at higher C-rates. However, it occurs independently of the cathode coating thickness and does not explain the falling trend seen here for electrodes with higher mass loading.

3.3.3 Structure analysis. The structural integrity of the lignin/water-based cathode surface is an important consideration when comparing the blade structures to the structures created using the silicon wafer as a stamp. These surface structures before and after cycling are shown in Fig. 13. Since the cathodes were structured when they were half-dried, the ceramic blade structures (BladePerf-LL) were more reproducible than the silicon wafer, as the former allowed for proper solvent evaporation during structuring. Unlike the ceramic blades, which only were in contact with the cathode surface at the indentation area, the silicon wafer acted like a stamp and covered the entire surface during structuring, which blocked the solvent evaporation. This induced additional challenges when structuring with the silicon wafer. Although the small lines (SL) and large lines (LL) were generally produced with high repeatability, challenges arose when using the silicon wafer to structure small pits (SP) and large pits (LP). Pit structures are more prone to collapse, and the extensive crack formations are shown in Fig. S3.† Fig. 13l also shows how the silicon wafer moved during compression and resulted in failure. This caused the higher standard deviations for the pit structures in Fig. 11f.

The dimensions of the mechanically structured lines before and after cycling are summarized in Table S8.†

The SEM analysis of the dimensions of the mechanically structured lignin/water cathodes in Fig. 12 shows a structure change during cycling. The small changes in the width of the lines may be caused by forming a CEI layer on the surface and volume expansions occurring during cycling. The structural post-mortem analysis shows increasing structural changes with higher mass loadings and porosities, as found for the PVDF/NMP cathodes discussed in Subsubsection 3.2.1.
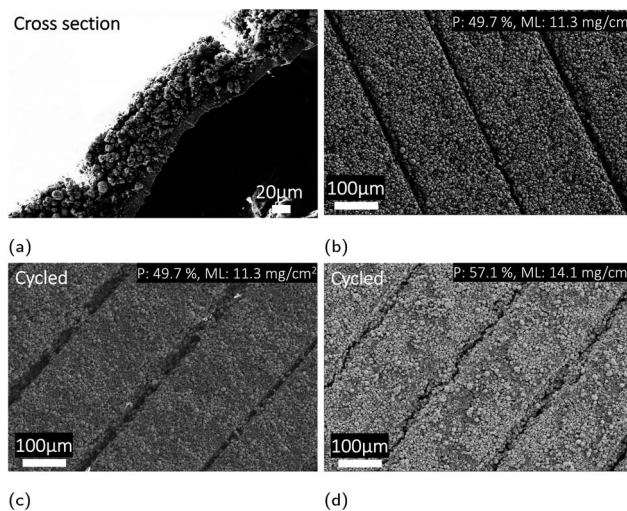

Fig. 12 SEM analysis of the lignin/water-based NMC cathodes mechanically perforated using ceramic blade creating large lines (BladePerf-LL). This cathode was a 60 μm thick cathode with ≈30 μm thick line indentations. (a) Pristine cross-section, (b) pristine cathode surface, and (c) and (d) post-mortem (after 54 cycles). The porosity (P) and mass loading (ML) were P: 49.7%, ML: 11.29 g cm^{-2} for (a–c), and P: 57.1%, ML: 14.14 mg cm^{-2} for (d).

No residual formations or destructive NMC111 particles are detected towards the mechanically structured lines or pits, which confirms that the laser beam induces these features.
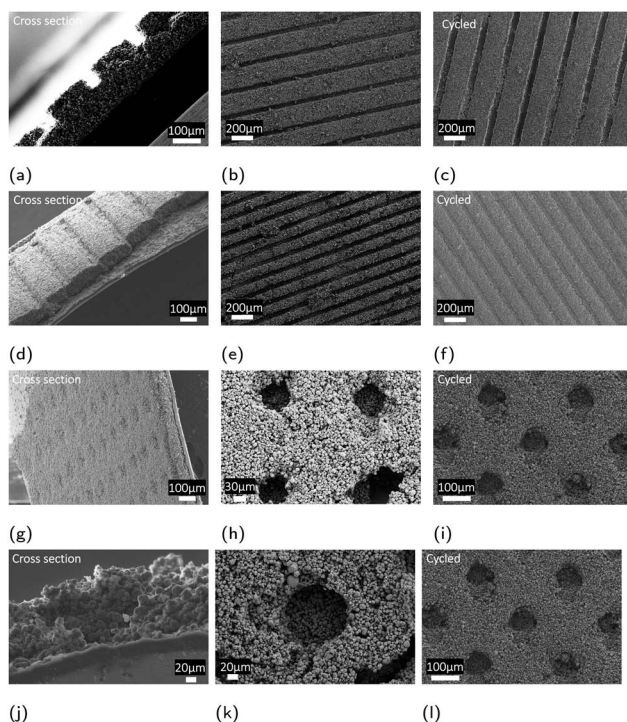

Fig. 13 SEM analysis of the structures fabricated using the silicon wafer: (a–c) large lines (LL), (d–f) small lines (SL), (g–i) small pits (SP), and (j–l) large pits (LP). Images to the left are the pristine cross-section; in the middle is the pristine electrode surface to the right is the electrode surface post-mortem (after 54 cycles). Image (l) is an example of a manufacturing error during manual mechanical structuring. Note that the image scale bars differ.

An EDS analysis was also conducted on the mechanically structured lignin/water-based cathodes after the rate test (54 cycles) in Table S1.† When comparing the elemental scan of the unstructured lignin/water-cathode to the different structure patterns (SL, LL, SP, LP, BladePerf-LL), no significant difference was detected. It should be mentioned that chromium (Cr) is a contaminant from the silicon wafer. The Cr concentration was highest for the LL cathode because this was structured first after the wafer fabrication. During usage, the Cr is effectively removed from the silicon wafer, and all of the cycled cathodes presented in this paper had a Cr <0.03%.

The elemental mapping from EDS in Table S1† shows an indication of transition metal (TM) leaching of Ni and Mn during cycling of lignin/water-cathodes, as the wt% ratio of Co is generally larger than Ni and Mn. However, by normalizing these values according to at% (Table S2†), the change after cycling is within the standard variation for all cathodes when comparing cycled and uncycled water-exposed cathodes; thus, the TM dissolution during cycling of NMC111 is negligible.[25,78] The same applies to the cycled mechanically structured lignin/water-based cathodes. However, the relative change may be smaller than the sensitivity of EDS, and a more accurate technique (ICP-MS) can be used to observe TM dissolution more accurately.[28,79]

Since PVDF is not present in these lignin-based cathodes, the F and P originate from the deposited CEI surface layer. The F and P concentration (wt%) in Table S1† increases from 0.20% to 9.83% and from 0% to 2.51%, respectively, after cycling. When comparing the EDS scan of the particles in PVDF/NMP-cathodes (Table S6†) to the surface mapping for lignin/water-cathodes (Table S1†), the overall wt% of P was higher for the PVDF cathodes compared to the lignin cathodes (1.3–2.53%). This is likely due to the residuals caused by the laser structuring of the PVDF cathodes, as mentioned earlier. This indicates that lignin does not present any negative effects on the overall CEI formation, and provides the cathode with not only sufficient mechanical stability but also electrochemical stability during cycling.

3.4 Comparison of lignin/water and PVDF/NMP cathodes

The discharge curves of unstructured and structured medium mass loading PVDF/NMP and lignin/water cathodes with similar mass loading (M-ML = 13.3–13.5 mg cm^{-2}), thickness ($\sim$100 μm), and porosities (37.2–41.3%) are presented in Fig. 14. No significant difference was detected in the initial discharge capacities at 0.1C, when comparing NMP-processed cathodes in Fig. 14a with the water-processed cathodes in Fig. 14c. This is in accordance with recent findings for water-processed NMC111, and NMC811 cathodes.[24]

The structured lignin/water-cathode with medium mass loading in Fig. 14d obtain a shortened voltage plateau in the first cycle. When decreasing the mass loading to 3.5 mg cm^{-2} (Fig. 14c) or changing the binder to PVDF (Fig. 14a), this plateau disappears. This feature is assigned to the poor electrolyte-wetting abilities of lignin, as discussed in our previous paper on lignin-based cathodes.[30] Poor wetting can prevent all pores from
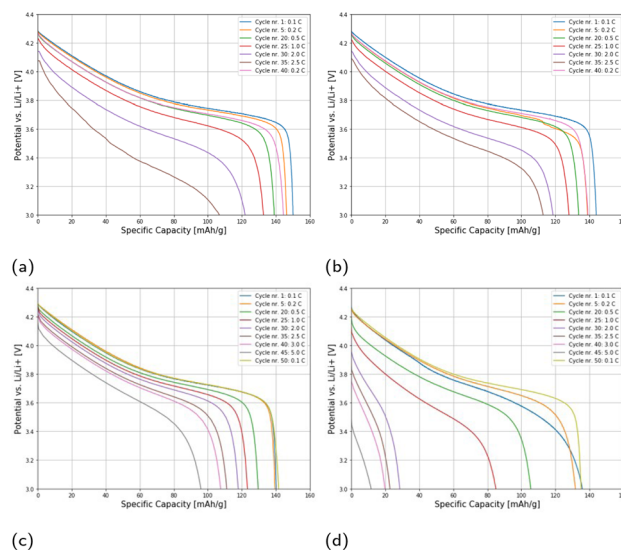

Fig. 14 Specific discharge capacity plots for unstructured and blade-structured cathodes with PVDF/NMP or lignin/water as binder/solvent. (a), (b) and (d) has medium mass loading (L-ML = 13.3–13.5 mg cm^{-2}), and (c) has low mass loading (L-ML = 3.5 mg cm^{-2}). (a) Unstructured PVDF/NMP, M-ML: T: 99 μm, P: 40.1%. (b) BladePerf-VLL PVDF/NMP, M-ML: T: 96 μm, P: 37.2%. (c) Unstructured lignin/water, L-ML: 28 μm, P: 44.4%. (d) BladePerf-LL structured lignin/water, M-ML: 99 μm, P: 41.3%.

properly filling with the electrolyte and leave some areas in the coating inactive. However, the voltage plateau usually disappears within the first four formation cycles for these 90 : 5 : 5 cathodes wetted for 6 days.

The NMP-exposed cathodes outperform those exposed to water at C-rates >0.2C. The specific capacity at 2.5C was 113 mA h g^{-1} and 22 mA h g^{-1} for the structured PVDF/NMP-based and lignin/water-based cathodes in Fig. 14b and d, respectively.

Multiple mechanisms can explain the increased lower rate capability for lignin/water-based cathodes relative to the PVDF/NMP-based cathodes. Since differences are only detected at high C-rates, the declining rate capability is likely caused by an increased surface resistance. This surface resistance may arise due to the binder chemistry, a different mixing procedure causing higher homogeneity, or increased NMC111 particle coverage.[21–24,78]

The lignin binder's long molecular chains can increase the tortuosity in the cathode coating or create further electrolyte decomposition reactions. A previous paper published on NMC111 cathodes using lignin as a binder by Bryntesen et al.[30] showed a cyclic voltammetry scan and a relatively high oxidation current within the potential window of the electrolyte in the first cycle when the lignin binder was exposed to the same electrolyte used here (LiPF$_6$ salt in the EC/DMC/DEC). There are also NaOH and Na$_2$S surface residuals associated with the lignin binder which may increase the resistance in the CEI and SEI layer formation (Table S1†).

When increasing the C-rate, a larger portion of the reactions occur on the surface of NMC111 rather than the bulk due to slow Li$^+$-diffusion into the bulk material. The resistivity induced

This journal is © The Royal Society of Chemistry 2023

J. Mater. Chem. A, 2023, **11**, 6483–6502 | **6499**

by surface contaminants is no longer negligible at higher discharge current densities and may partly explain why the water-exposed NMC111 suffers from lower cycling capacity at increased C-rates.[24] Although there were no extra Li_2CO_3 and LiOH layers present on the surface of water-exposed NMC111 particles according to XPS measurements from our previous article,[30] the presence of residual H^+ from the Li^+/H^+ exchange caused by Li^+-leaching, the NaOH and N_2S from the lignin, or the lignin binder itself may form a thicker resistance layer around the particles and may become visible as a drop in capacity when increasing the discharge current densities >0.1 C.

Another reason known to affect the electrochemical performance of aqueous processed batteries is the post-drying temperature (120 °C) before cell assembly.[25] If the temperature is not sufficiently high to completely remove residual moisture from the pores in the lignin/water-based cathodes, a decomposition reaction occurs between water molecules and the supporting lithium hexafluorophosphate ($LiPF_6$) salt. This reaction generates hydrogen fluoride (HF). HF is necessary to passivize the Al current collector but may be detrimental for the oxides.[80] Karl-Fischer titration experiments may be included in future experiments to reveal the moisture content, and the residual humidity of the water-based NMC111 cathodes.[25] However, others[81] have found that post-drying at 120 °C was sufficient to remove the moisture, and we believe the moisture content was equal in both NMP- and water-fabricated cells. Thus, H^+ residuals from the Li^+/H^+-exchange in NMC111 particles are the only potential species which may contribute to HF formation. However, it should be mentioned that residual water tends to affect the initial capacity and long-term cyclability, rather than only the rate performance as seen here.[25]

The results demonstrate how the porosity optimization and structuring of the cathode surface can increase the performance of both lignin/water and PVDF/NMP-based cathodes. To fully replace the PVDF/NMP with lignin/water, the mechanisms causing the inferior rate performance for the latter should be further investigated. One way of increasing the reliability of the water-based lignin binder can be to eliminate the errors related to the water-sensitivity of the NMC111 by replacing this active material with water-compatible materials such as graphite or LFP.

4 Conclusion

• By decreasing the electrode's mass loading with a factor of three (14.5 to 4.7 mg cm^{-2}), the laser structuring method's waste material was halved. This indicates that the laser structuring becomes more efficient for the forthcoming ultra-thick electrodes.

• The laser structuring method produced structures of higher precision and accuracy compared to the mechanically structured cathodes.

• The mechanical methods (blade and silicon wafer structuring) showed no waste material and surface residual formation.

• The rate capability decreased with a higher cathode mass loading but was improved with calendering and mechanical and laser surface structuring for both PVDF/NMP and lignin/water-fabricated cathodes.

• Lignin/water-fabricated cathodes up to a thickness of 150 μm were fabricated successfully, but extensive degradation occurred during cycling when reaching thicknesses ~200 μm as the capacity were not retained after cycling.

• For the lignin/water-based cathodes, the mechanically structured large lines (LL) using ceramic blades enabled the highest discharge capacity at high C-rates and was preferred over the stamp-like silicon wafer structuring method. The former provided easier solvent evaporation pathways during drying and; thus, higher mechanical stability. At a thickness of 150 μm, the rate capability of lignin/water-cathodes was only improved for the line structures created using ceramic blades.

• Mechanically structured lines were preferred over pits as they obtained higher reproducibility and mechanical stability.

• Comparing the rate capability of calendered and uncalendered with and without surface structures showed that structuring pore channels into a dense calendered electrode surface are preferred over keeping the bulk porosity high by avoiding calendering since the induced pore channels enables a high ionic conductivity without sacrificing the electrical conductivity.

• Structuring is preferred on dense calendered electrodes, as surface cracks and high porosity reduces the mechanical integrity of the structures during cycling.

• The PVDF/NMP and lignin/water-cathodes showed similar capacity at low C-rates (C/10). At higher C-rates, the lignin/water-based cathodes generally showed lower capacity retention. The difference in fabrication parameters makes comparison difficult, but the decrease in rate capability for lignin/water-based cathodes was likely a combination of an improved binder-coverage on the NMC111 particles, an additional resistance induced by NaOH and Na_2S, the presence of water or water-exposure of NMC111, and the poor electrolyte wettabilities for lignin.

Author contributions

O. S. B.: writing – review and editing, supervision, conceptualization, project administration, funding acquisition. A. M. S.: writing – review and editing, supervision, validation. J. J. L.: writing – review and editing, supervision, validation. P. R. S.: writing – review and editing, supervision, validation. P. H. F.: data curation, formal analysis. S. N. B.: methodology, investigation, data curation, formal analysis, conceptualization, writing – original draft. J. V.: data curation, formal analysis. I. T. S.: project administration, writing – review and editing. N. T.: data curation, formal analysis, writing – review and editing.

Conflicts of interest

There are no conflicting interests to declare.

6500 | J. Mater. Chem. A, 2023, 11, 6483–6502

This journal is © The Royal Society of Chemistry 2023

Acknowledgements

Notes and references

1 S. N. Bryntesen, A. H. Strømman, I. Tolstorebrov, P. R. Shearing, J. J. Lamb and O. Stokke Burheim, *Energies*, 2021, **14**, 1406.

2 J. Li, Y. Lu, T. Yang, D. Ge, D. L. Wood and Z. Li, *iScience*, 2020, **23**, 101081.

3 R. Sahore, M. Wood, A. Kukay, Z. Du, K. M. Livingston, D. L. Wood and J. Li, *J. Electrochem. Soc.*, 2022, **169**, 040567.

4 D. L. Wood, J. D. Quass, J. Li, S. Ahmed, D. Ventola and C. Daniel, *Drying Technol.*, 2018, **36**, 234–244.

5 S.-L. Chou, Y. Pan, J.-Z. Wang, H.-K. Liu and S.-X. Dou, *Phys. Chem. Chem. Phys.*, 2014, **16**, 20347.

6 T. C. Nirmale, B. B. Kale and A. J. Varma, *A Review on Cellulose and Lignin Based Binders and Electrodes: Small Steps towards a Sustainable Lithium Ion Battery*, 2017.

7 D. Bresser, D. Buchholz, A. Moretti, A. Varzi and S. Passerini, *Energy Environ. Sci.*, 2018, **11**, 3096–3127.

8 Y. Ma, J. Ma and G. Cui, *Energy Storage Mater.*, 2019, **20**, 146.

9 V. Ponnuchamy and E. S. Esakkimuthu, *Appl. Surf. Sci.*, 2022, **573**, 151461.

10 Y. Li, *IOP Conf. Ser.: Earth Environ. Sci.*, 2020, **514**, 042019.

11 I. Doberdò, N. Löffler, N. Laszczynski, D. Cericola, N. Penazzi, S. Bodoardo, G. T. Kim and S. Passerini, *J. Power Sources*, 2014, **248**, 1000–1006.

12 F. S. Chakar and A. J. Ragauskas, *Ind. Crops Prod.*, 2004, **20**, 131–141.

13 V. K. Thakur, M. K. Thakur, P. Raghavan and M. R. Kessler, *ACS Sustainable Chem. Eng.*, 2014, **2**, 1072–1092.

14 S. Kane, R. Ulrich, A. Harrington, N. P. Stadie and C. Ryan, *Carbon Trends*, 2021, **5**, 100088.

15 D. Kai, M. J. Tan, P. L. Chee, Y. K. Chua, Y. L. Yap and X. J. Loh, *Green Chem.*, 2016, **18**, 1175–1200.

16 W. O. Doherty, P. Mousavioun and C. M. Fellows, *Ind. Crops Prod.*, 2011, **33**, 259–276.

17 W. Li, Y. Zhang, L. Das, Y. Wang, M. Li, N. Wanninayake, Y. Pu, D. Y. Kim, Y. T. Cheng, A. J. Ragauskas and J. Shi, *RSC Adv.*, 2018, **8**, 38721–38732.

18 S. D. Gong, Y. Huang, H. J. Cao, Y. H. Lin, Y. Li, S. H. Tang, M. S. Wang and X. Li, *J. Power Sources*, 2016, **307**, 624–633.

19 H. Lu, A. Cornell, F. Alvarado, M. Behm, S. Leijonmarck, J. Li, P. Tomani and G. Lindbergh, *Materials*, 2016, **9**, 127.

20 W. E. Tenhaeff, O. Rios, K. More and M. A. McGuire, *Adv. Funct. Mater.*, 2014, **24**, 86–94.

21 M. Wood, J. Li, R. E. Ruther, Z. Du, E. C. Self, H. M. Meyer, C. Daniel, I. Belharouak and D. L. Wood, *Energy Storage Mater.*, 2020, **24**, 188–197.

22 F. A. Çetinel and W. Bauer, *Bull. Mater. Sci.*, 2014, **37**, 1685–1690.

23 X. Zhang, W. J. Jiang, X. P. Zhu, A. Mauger, Qilu and C. M. Julien, *J. Power Sources*, 2011, **196**, 5102–5108.

24 L. Azhari, X. Zhou, B. Sousa, Z. Yang, G. Gao and Y. Wang, *ACS Appl. Mater. Interfaces*, 2020, **12**, 57963–57974.

25 M. Memm, A. Hoffmann and M. Wohlfahrt-Mehrens, *Electrochim. Acta*, 2018, **260**, 664–673.

26 P. Zhu, J. Han and W. Pfleging, *Nanomaterials*, 2021, **11**, 1840.

27 R. Jung, R. Morasch, P. Karayaylali, K. Phillips, F. Maglia, C. Stinner, Y. Shao-Horn and H. A. Gasteiger, *J. Electrochem. Soc.*, 2018, **165**, A132.

28 W. B. Hawley, A. Parejiya, Y. Bai, H. M. Meyer, D. L. Wood and J. Li, *J. Power Sources*, 2020, **466**, 228315.

29 I. A. Shkrob, J. A. Gilbert, P. J. Phillips, R. Klie, R. T. Haasch, J. Bareño and D. P. Abraham, *J. Electrochem. Soc.*, 2017, **164**, A1489–A1498.

30 S. N. Bryntesen, O. Burheim and J. Lamb, *ECS Meeting Abstr.*, 2022, **1**, 2425.

31 M. Ragnar, C. T. Lindgren and N.-O. Nilvebrant, *J. Wood Chem. Technol.*, 2000, **20**, 277–305.

32 H. Buqa, M. Holzapfel, F. Krumeich, C. Veit and P. Novák, *J. Power Sources*, 2006, **161**, 617–622.

33 A. M. Boyce, D. J. Cumming, C. Huang, S. P. Zankowski, P. S. Grant, D. J. Brett and P. R. Shearing, *ACS Nano*, 2021, **15**, 18624–18632.

34 K. Rollag, D. Juarez-Robles, Z. Du, D. L. Wood and P. P. Mukherjee, *ACS Appl. Energy Mater.*, 2019, **2**, 4464–4476.

35 Z. Du, K. M. Rollag, J. Li, S. J. An, M. Wood, Y. Sheng, P. P. Mukherjee, C. Daniel and D. L. Wood, *J. Power Sources*, 2017, **354**, 200–206.

36 T. P. Plateau, H. Pham, Y. Zhu, M. Leu and J. Park, *Adv. Energy Mater.*, 2022, **12**, 2201353.

37 W. Pfleging and J. Pröll, *J. Mater. Chem. A*, 2014, **2**, 14918–14926.

38 J. Hu, B. Wu, X. Cao, Y. Bi, S. Chae, C. Niu, B. Xiao, J. Tao, J. Zhang and J. Xiao, *J. Power Sources*, 2020, **454**, 227966.

39 H. Zheng, L. Tan, G. Liu, X. Song and V. S. Battaglia, *J. Power Sources*, 2012, **208**, 52–57.

40 J. Habedank, M. Zäh and A. Kwade, *Laser Structuring of Graphite Anodes for Functionally Enhanced Lithium-Ion Batteries*, Universitätsbibliothek der TU München, 2021.

41 J. Billaud, F. Bouville, T. Magrini, C. Villevieille and A. R. Studart, *Nat. Energy*, 2016, **1**(8), 1–6.

42 J. S. Sander, R. M. Erb, L. Li, A. Gurijala and Y. M. Chiang, *Nat. Energy*, 2016, **1**(8), 1–7.

43 L. Li, R. M. Erb, J. Wang, J. Wang and Y. M. Chiang, *Adv. Energy Mater.*, 2019, **9**, 1802472.

44 B.-S. Lee, Z. Wu, V. Petrova, X. Xing, H.-D. Lim, H. Liu and P. Liu, *J. Electrochem. Soc.*, 2018, **165**, A525–A533.

45 B. Delattre, R. Amin, J. Sander, J. De Coninck, A. P. Tomsia and Y. M. Chiang, *J. Electrochem. Soc.*, 2018, **165**, A388–A395.

This journal is © The Royal Society of Chemistry 2023

J. Mater. Chem. A, 2023, **11**, 6483–6502 | **6501**

46 S. Behr, R. Amin, Y.-M. Chiang and A. P. Tomsia, *Ceram. Forum Int.*, 2015, **92**, E39–E43.

47 C. Huang and P. S. Grant, *J. Mater. Chem. A*, 2018, **6**, 14689–14699.

48 R. Amin, B. Delattre, A. P. Tomsia and Y. M. Chiang, *ACS Appl. Energy Mater.*, 2018, **1**, 4976–4981.

49 Z. Liu, T. W. Verhallen, D. P. Singh, H. Wang, M. Wagemaker and S. Barnett, *J. Power Sources*, 2016, **324**, 358–367.

50 S. Zhang, Y. Liu, M. Qi and A. Cao, *Acta Phys.-Chim. Sin.*, 2020, **37**, 2011007.

51 C. L. Cobb and S. E. Solberg, *J. Electrochem. Soc.*, 2017, **164**, A1339–A1341.

52 F. L. Usseglio-Viretta, W. Mai, A. M. Colclasure, M. Doeff, E. Yi and K. Smith, *Electrochim. Acta*, 2020, **342**, 136034.

53 P. Smyrek, Y. Zheng, H. J. Seifert and W. Pfleging, *Laser-based Micro Nanoprocessing X*, 2016, **9736**, 97361C.

54 A. C. Wagner, N. Bohn, H. Geßwein, M. Neumann, M. Osenberg, A. Hilger, I. Manke, V. Schmidt and J. R. Binder, *ACS Appl. Energy Mater.*, 2020, **3**, 12565–12574.

55 L. Hille, H.-C. Toepper, C. Schriever, J. Kriegler, J. Keilhofer, M. P. Noecker and M. F. Zaeh, *J. Electrochem. Soc.*, 2022, **169**, 060518.

56 V. P. Nemani, S. J. Harris and K. C. Smith, *J. Electrochem. Soc.*, 2015, **162**, A1415.

57 N. Dunlap, D. B. Sulas-Kern, P. J. Weddle, F. Usseglio-Viretta, P. Walker, P. Todd, D. Boone, A. M. Colclasure, K. Smith, B. J. Tremolet de Villers and D. P. Finegan, *J. Power Sources*, 2022, **537**, 231464.

58 L. Hille, L. Xu, J. Keilhofer, S. Stock, J. Kriegler and M. F. Zaeh, *Electrochim. Acta*, 2021, **392**, 139002.

59 M. Mangang, H. J. Seifert and W. Pfleging, *J. Power Sources*, 2016, **304**, 24–32.

60 T. Tsuda, N. Ando, S. Nakamura, Y. Ishihara, N. Hayashi, N. Soma, T. Gunji, T. Tanabe, T. Ohsaka and F. Matsumoto, *Electrochim. Acta*, 2019, **296**, 27–38.

61 T. Tsuda, N. Ando, K. Matsubara, T. Tanabe, K. Itagaki, N. Soma, S. Nakamura, N. Hayashi, T. Gunji, T. Ohsaka and F. Matsumoto, *Electrochim. Acta*, 2018, **291**, 267–277.

62 J. Pröll, H. Kim, A. Piqué, H. J. Seifert and W. Pfleging, *J. Power Sources*, 2014, **255**, 116–124.

63 P. Zhu, H. J. Seifert and W. Pfleging, *Appl. Sci.*, 2019, **9**, 4067.

64 J. Park, C. Jeon, W. Kim, S. J. Bong, S. Jeong and H. J. Kim, *J. Power Sources*, 2021, **482**, 228948.

65 F. Duffner, L. Mauler, M. Wentker, J. Leker and M. Winter, *Int. J. Prod. Econ.*, 2021, **232**, 107982.

66 J. Park, H. Song, I. Jang, J. Lee, J. Um, S.-G. Bae, J. Kim, S. Jeong and H.-J. Kim, *J. Energy Chem.*, 2022, **64**, 93–102.

67 W. Pfleging, *Nanophotonics*, 2017, **7**, 549–573.

68 I. T. Sorokina, *Next generation mid-infrared lasers: a route towards sub-wavelength 3D manufacturing*, OPIC'22, Japan, 2022.

69 N. Tolstik, E. Sorokin, J. C. Mac-Cragh, R. Richter and I. T. Sorokina, *Conference on Lasers and Electro-Optics (2022), Paper AM4I.8*, 2022.

70 X. Zhang and T. M. Devine, *J. Electrochem. Soc.*, 2006, **153**, B365.

71 P. Zhu, D. Gastol, J. Marshall, R. Sommerville, V. Goodship and E. Kendrick, *J. Power Sources*, 2021, **485**, 229321.

72 A. G. Blackman, *Aylward and Findlay's SI Chemical Data*, Wiley, 7th edn, 2014.

73 C. Ronchi, R. Beukers, H. Heinz, J. P. Hiernaut and R. Selfslag, *Int. J. Thermophys.*, 1992, **13**, 107–129.

74 J. Steinbeck, G. Braunstein, M. S. Dresselhaus, T. Venkatesan and D. C. Jacobson, *J. Appl. Phys.*, 1985, **58**, 4374–4382.

75 C. Busà, M. Belekoukia and M. J. Loveridge, *Electrochim. Acta*, 2021, **366**, 137358.

76 N. Phattharasupakun, P. Bunyanidhi, P. Chiochan, N. Chanlek and M. Sawangphruk, *Electrochem. Commun.*, 2022, **139**, 107309.

77 S. S. Choi and H. S. Lim, *J. Power Sources*, 2002, **111**, 130–136.

78 N. Loeffler, G. T. Kim, F. Mueller, T. Diemant, J. K. Kim, R. J. Behm and S. Passerini, *ChemSusChem*, 2016, **9**, 1112–1117.

79 J. A. Gilbert, I. A. Shkrob and D. P. Abraham, *J. Electrochem. Soc.*, 2017, **164**, A389–A399.

80 M. Yamada, T. Watanabe, T. Gunji, J. Wu and F. Matsumoto, *Electrochem*, 2020, **1**, 124–159.

81 J. Li, C. Daniel, S. J. An and D. Wood, *MRS Adv.*, 2016, 1029–1035.

6502 | *J. Mater. Chem. A*, 2023, **11**, 6483–6502

This journal is © The Royal Society of Chemistry 2023